

Article

Multi-Objective Topology Optimization of Conjugate Heat Transfer Using Level Sets and Anisotropic Mesh Adaptation

Philippe Meliga¹, Wassim Abdel Nour^{1,2} , Delphine Laboureur³, Damien Serret² and Elie Hachem^{1,*}

¹ Mines Paris, PSL University, Centre for Material Forming (CEMEF), UMR CNRS, 06904 Sophia Antipolis, France

² TEMISTh SAS, Technocentre des Florides, 13700 Marignane, France

³ The von Karman Institute for Fluid Dynamics, Waterloosesteenweg 72, B-1640 Sint-Genesius Rode, Belgium

* Correspondence: elie.hachem@minesparis.psl.eu; Tel.: +33-4-93-95-74-58

Abstract: This study proposes a new computational framework for the multi-objective topology optimization of conjugate heat transfer systems using a continuous adjoint approach. It relies on a monolithic solver for the coupled steady-state Navier–Stokes and heat equations, which combines finite elements stabilized by the variational multi-scale method, level set representations of the fluid–solid interfaces and immersed modeling of heterogeneous materials (fluid–solid) to ensure that the proper amount of heat is exchanged to the ambient fluid by solid objects in arbitrary geometry. At each optimization iteration, anisotropic mesh adaptation is applied in near-wall regions automatically captured by the level set. This considerably cuts the computational effort associated with calling the finite element solver, in comparison to traditional topology optimization algorithms operating on isotropic grids with a comparable refinement level. Given that we operate within the constraint of a specified number of nodes in the mesh, this allows not only to improve the accuracy of interface representation and motion but also to retain the high fidelity of the numerical solutions at the grid points just adjacent to the interface. Finally, the remeshing and resolution steps both run within a highly parallel environment, which makes it possible for the proposed algorithm to tackle large-scale problems in three dimensions with several tens of millions of state degrees of freedom. The developed solver is validated first by minimizing dissipation in a flow splitter device, for which the method delivers relevant optimal designs over a wide range of volume constraints and flow rate distributions over the multiple outlet orifices but yields better accuracy compared to reference data from literature obtained using uniform meshes (in the sense that the layouts are more smooth, and the solutions are better resolved). The scheme is then applied to a two-dimensional heat transfer problem, using bi-objective cost functionals combining flow resistance and thermal recoverable power. A comprehensive parametric study reveals a complex arrangement of optimal solutions on the Pareto front, with multiple branches of symmetric and asymmetric designs, some of them previously unreported. Finally, the algorithmic developments are substantiated with several three-dimensional numerical examples tackled under fixed weights for heat transfer and flow resistance, for which we show that the optimal layouts computed at low Reynolds number, that are intrinsically relevant to a broad range of microfluidic application, can also serve as smooth solutions to high-Reynolds-number engineering problems of practical interest.

Keywords: topology optimization; fluid mechanics; conjugate heat transfer; level set method; anisotropic mesh adaptation; Pareto front; thermal control



Citation: Meliga, P.; Abdel Nour, W.; Laboureur, D.; Serret, D.; Hachem, E. Multi-Objective Topology Optimization of Conjugate Heat Transfer Using Level Sets and Anisotropic Mesh Adaptation. *Fluids* **2024**, *9*, 105. <https://doi.org/10.3390/fluids9050105>

Academic Editor: Wei-Tao Wu

Received: 1 March 2024

Revised: 22 April 2024

Accepted: 24 April 2024

Published: 28 April 2024



Copyright: © 2024 by the authors. Licensee MDPI, Basel, Switzerland. This article is an open access article distributed under the terms and conditions of the Creative Commons Attribution (CC BY) license (<https://creativecommons.org/licenses/by/4.0/>).

1. Introduction

Topology optimization is the mathematical science of optimal material allocation in a volume under predefined objectives and constraints. This methodology has its roots in solid mechanics [1,2] but has evolved into a potent, dependable, and more accessible resource for engineers during the initial phases of intricate structural design processes [3,4]. It has also

extended to numerous multiphysics scenarios governed by partial differential equations, with an overview of the developing techniques and applications available in Refs [5,6]. The mathematical underpinnings of topology optimization stem from iterative analysis and design update procedures, frequently guided by gradient computations. Unlike the classical size and shape optimization methods from which it is derived, its primary benefit lies in its ability to typically exceed expectations, as there is no complexity restriction on the resulting design, which can allow to encompass conflicting demands and intricate interdependencies among design parameters.

In the context of fluid flow problems, topology optimization becomes a question of where in a predetermined domain to enforce relevant boundary conditions for the flow problem so as to find what constitutes the optimal way for the fluid to flow. The density and level set methods have emerged as the two dominant techniques for this purpose (one can also utilize explicit boundary methods, in which the fluid–solid interface is discretized by the edges or faces of a body-fitted mesh, but those are constrained in their ability to manage complex topological alterations). In density methods, a Brinkman penalization approach is used inside the solid, which amounts to representing the flow therein as a fictitious porous material with extremely low permeability [1,7,8]. Such methods can accommodate significant topological alterations (given that the sensitivity/gradient information is distributed across a whole domain) but may result in fluid leaking out of the desired area if the penalization factor is not properly calibrated. In contrast, level set techniques use the iso-contours of level set (distance) functions to capture all solid boundaries [9–11], in which case the gradient information is available only at the interface between the solid and fluid domains. Such methods therefore lack a mechanism for nucleating new holes (which is matched by including numerous holes in the initial designs), but they facilitate well-defined, sharp interface representations and adeptly handle intricate topological modifications such as hole merging or cancellation. In addition, they avoid the classical pitfalls of density methods, that generally suffer from staircasing (a phenomenon by which curved surfaces are discretized into stair steps that gives rise to unwanted mesh-dependent spatial oscillations of the interface representation) and rely on intermediate material phases (grayscale elements) that do not have a clear physical interpretation [12].

The focus here is on conjugate convective heat transfer systems, in which temperature variations occur within the fluid and solid material due to thermal interactions dominated by conduction in the solid and convection in the fluid. This is a matter of great engineering interest, as many industries have embraced the ability of topology optimization to improve the performance and cut the production costs of thermal devices like heat exchangers (to regulate process temperatures and ensure that chemicals, machinery, food, drugs or gas stay in safe operating ranges), finned surfaces, microelectronic equipment, and heat sinks, and to deliver more streamlined designs involving low friction and mass but high thermal performance. Early on, the literature related to this topic could be broken down into the following two groups: those problems focused solely on heat conduction that maximize heat evacuation from singular tree-like optimal structures of high conduction material, and those problems focused on reducing the energy footprint (flow resistance) of complex channel layouts in the diffusion and convection dominated regimes. See [13,14] for recent reviews and references therein. Since then, the topology optimization of coupled thermal–fluid problems (that combine both aspects, and thus require dual objective function strategies to maximize the thermal performance while minimizing the flow resistance) has become an active field of research. Although variants of the level set method have received attention recently [15–17], the vast majority of available studies implement a density-based monolithic approach [18–26] to overcome the fact that the fluid–solid interface is constantly changing over the optimization process, which makes it difficult to model the heat transfer between the fluid and its surrounding from some heat transfer coefficient or surrogate model. A variety of models have been used, ranging from oversimplified (dismissing the difference in the fluid–solid thermal conductivities [22] or numerically imposing a constant

solid temperature [21]), to highly realistic (full coupling of flow and heat transfer under dual objective function strategies [18]).

In topology optimization, it is customary to utilize fixed finite element meshes with uniform (or nearly) element sizes. These sizes are chosen to be small enough to accurately capture all key physical phenomena, yet not so small as to render the optimization process prohibitively expensive. A recent trend in the field involves employing adaptive remeshing techniques that entail generating a coarse base grid and subsequently progressively refining the mesh elements in regions demanding a higher resolution. This process repeats until a maximum level of refinement is achieved, or (in sophisticated implementations with error estimation capabilities) the local truncation error falls below a user-defined tolerance level. As far as pure fluid flow problems are concerned, significant attention has been given to adaptive meshing refinement (AMR) schemes, in the realm of both density methods [27,28] and level set techniques [29,30]. An application to phase field modeling (another capturing method solving interfacial problems that has recently become popular for simulating immiscible two-phase flows) can be found in [31]; see also [32,33] for an application of different remeshing techniques to a blend of level sets and body-fitted meshes in the context of convective heat transfer and other coupled physics models.

Despite the progress made thus far, nearly all adaptive algorithms applied to fluid flow topology optimization rely on isotropic metric maps. Meanwhile, fluid dynamics inherently involves the numerical simulation of convection-dominated problems for which the ability to use extremely stretched mesh elements is highly valuable, especially in boundary layer regions where skin friction driven by steep gradients in the wall-normal fluid velocity is essential [34]. The premise of our study is that there is great interest in using anisotropic metric maps optimally suited to the solid–fluid interfaces. This has potential to enhance the accuracy of the geometric representation and that of the numerical solutions without resorting to advanced interpolation or discretization methods, which aligns perfectly with recommendations made in [14] to advance the current state of the art. For all that, we could not find in the literature any research attempting to meet the demands of automatic anisotropic mesh adaptation for topology optimization in thermal–fluid problems, for which possible explanations are the lack of monolithic conjugate heat transfer solvers, and the difficulty of finding spatial discretization schemes exhibiting a sufficient robustness level (for context, the density-based optimization of Stokes flow in [28] does use anisotropic meshes but leaves aside convection-dominated phenomena and thermal coupling).

In order to address this gap, this study proposes an original numerical framework capable of effectively tackle the topology optimization of conjugate heat transfer problems, thanks to a combination of level set techniques and anisotropic mesh adaptation that makes it possible to accurately handle and evolve arbitrary geometries immersed in an unstructured mesh. A variational multi-scale (VMS) stabilized finite element method capable of handling extremely narrow mesh elements with aspect ratios of up to 1000:1 [35] is used to solve all equations, that is, the governing, coupled Navier–Stokes and heat equations, as well as the adjoint coupled equations needed to evolve the level set functions through relevant sensitivity analysis. Based on an anisotropic metric map constructed directly at the nodes of the mesh from the level set information, the mesh is adapted using an a posteriori error estimator that seeks to minimize the interpolation error while adhering to a user-defined number of nodes. Notably, this allows to dynamically adjust the mesh refinement throughout the optimization process, enabling the refinement or coarsening of the base grid as needed. This flexibility stands in contrast to AMR schemes, where the total number of mesh elements cannot be controlled, and further coarsening beyond the base configuration is not possible. Such an approach is anticipated to yield additional speed-ups by reducing the computational cost associated with modeling the solid material away from the interface, while also enhancing the manufacturability of the optimal design. This latter aspect is particularly pertinent, as traditional topology optimization algorithms tend to produce organic designs that can pose challenges when it comes to translating to computer-aided design (CAD) models.

The structure of the paper is as follows: the formulation of the topology optimization equations is provided in Section 2. Sections 3 and 4 detail the immersed, stabilized finite element framework and anisotropic mesh adaptation algorithm used to perform the design update step. The implementation details of the topology optimization algorithm are outlined in Section 5. Finally, numerical experiments showcasing the potential of the approach to increase the recoverable thermal power while minimizing the dissipated power in two dimensional (2-D) and three-dimensional (3-D) systems are presented in Section 6, with emphasis on showing the improved accuracy throughout the optimization process. Finally, the numerical cost is discussed in Section 7, where we also debate the generalization to high-Reynolds number regimes.

2. Gradient-Based Model for Conjugate Heat Transfer Topology Optimization

2.1. Governing Equations

In the ensuing discussion, let Ω be a fixed, open bounded domain in \mathbb{R}^d (where d denotes the space dimension), with its boundary $\partial\Omega$ oriented by the inward-pointing normal vector \mathbf{n} . Throughout this investigation, we consider Ω to be the union of two disjoint regions $\Omega = \Omega_f \cup \Omega_s$, comprising a fluid domain Ω_f and a solid domain Ω_s , respectively. These regions are separated by an interface $\Gamma = \Omega_f \cap \Omega_s$, the position of which we optimize with regard to a specific performance metric. The fluid domain boundary $\partial\Omega_f$ is divided into the interface and the collective boundaries of all surfaces through which fluid either enters or exits the domain, referred to as inlet Γ_i and outlet Γ_o , respectively. Similarly, the solid domain boundary $\partial\Omega_s$ is divided into the interface, and the collective boundaries of all surfaces where either temperature is specified, or heat is exchanged with no gain or loss, referred to as isothermal Γ_w^i and adiabatic Γ_w^a , respectively.

Mathematically, the problem is defined by a collection of physical variables that are established as solutions to partial differential equations (PDEs). These PDEs are derived from modeling considerations and serve as constraints throughout the optimization process. In the following, the interface between the fluid and solid domains is represented by the zero iso-value of a continuous level set function. Typically, this function is the signed distance function, defined as

$$\varphi(\mathbf{x}) = \begin{cases} -\text{dist}(\mathbf{x}, \Gamma) & \text{if } \mathbf{x} \in \Omega_f, \\ 0 & \text{if } \mathbf{x} \in \Gamma, \\ \text{dist}(\mathbf{x}, \Gamma) & \text{if } \mathbf{x} \in \Omega_s, \end{cases} \quad (1)$$

with the convention that $\varphi > 0$ (respectively, $\varphi < 0$) in the solid (respectively, the fluid) domain. The immerse volume method (IVM, more details in Section 3) is then used to extend to the whole domain Ω the coupled steady incompressible Navier–Stokes and heat equations governing the flow motion in the fluid domain Ω_f . Simply put, the IVM fills Ω_s with a fictitious fluid mimicking a solid phase but avoids introducing discontinuities at the interface. It then solves fluid-like equations in the whole domain Ω , using non-homogeneous material properties adequately interpolated over a small layer around the zero level set (whose thickness is specified by the user and remains constant throughout the optimization process, unlike in the homogenization method or any other generalized material method, where it may vary) and otherwise equal to their fluid and solid values. This yields the monolithic formulation

$$\nabla \cdot \mathbf{u} = 0 \quad \text{in } \Omega, \quad (2)$$

$$\rho \mathbf{u} \cdot \nabla \mathbf{u} = -\nabla p + \nabla \cdot (2\mu \boldsymbol{\varepsilon}(\mathbf{u})) \quad \text{in } \Omega, \quad (3)$$

$$\rho c_p \mathbf{u} \cdot \nabla T = \nabla \cdot (k \nabla T) \quad \text{in } \Omega, \quad (4)$$

where we denote by \mathbf{u} the velocity, p the pressure, $\boldsymbol{\varepsilon}(\mathbf{u}) = (\nabla \mathbf{u} + \nabla \mathbf{u}^T)/2$ the rate of the deformation tensor, and ρ, μ, k and c_p are the phase-dependent density, dynamic viscosity, thermal conductivity and specific heat.

We seek here to minimize a cost function J that we assume can be formulated as a surface (rather than volume) integral over all or any part of the inlet and/or outlet (as is most often the case in topology optimization), i.e.,

$$J_s = \int_{\Gamma_i \cup \Gamma_o} J ds. \tag{5}$$

This is performed using the continuous adjoint method to find the cost function sensitivity to variations of a design variable β physically representing local surface normal displacements of the interface. In brief, the intended sensitivity to a displacement β at a particular point on the interface is expressed as

$$\delta_\beta J_s = \int_\Gamma \beta \mu (\nabla \tilde{\mathbf{u}} \cdot \mathbf{n}) \cdot (\nabla \mathbf{u} \cdot \mathbf{n}) ds + \int_\Gamma \beta k (\nabla \tilde{T} \cdot \mathbf{n}) (\nabla T \cdot \mathbf{n}) ds, \tag{6}$$

with $\tilde{\mathbf{u}}$, \tilde{p} and \tilde{T} as the adjoint velocity, pressure and temperature fields, computed as the solutions to the coupled adjoint Navier–Stokes and heat equations, written in monolithic formulation as

$$\nabla \cdot \tilde{\mathbf{u}} = 0 \quad \text{in } \Omega, \tag{7}$$

$$-\rho \mathbf{u} \cdot \nabla \tilde{\mathbf{u}} + \rho \nabla \mathbf{u}^T \cdot \tilde{\mathbf{u}} = \nabla \tilde{p} + \nabla \cdot (2\mu \boldsymbol{\varepsilon}(\tilde{\mathbf{u}})) \quad \text{in } \Omega, \tag{8}$$

$$-c_p \mathbf{u} \cdot \nabla \tilde{T} = \nabla \cdot (k \nabla \tilde{T}) \quad \text{in } \Omega. \tag{9}$$

The main steps of the method are described in Appendix A, together with the boundary conditions appended to both the state and adjoint equations; see also [36–38] for further deepening on the topic. This allows to design efficient update procedures based on first-order gradient evaluations. For example, the baseline steepest-descent algorithm employed in this study uses

$$\beta = -\mu (\nabla \tilde{\mathbf{u}} \cdot \mathbf{n}) \cdot (\nabla \mathbf{u} \cdot \mathbf{n}) - k (\nabla \tilde{T} \cdot \mathbf{n}) (\nabla T \cdot \mathbf{n}), \tag{10}$$

to progress along the cost function up to a positive scaling factor to regulate the magnitude of the step taken in the direction of the steepest slope.

2.2. Multi-Objective Optimization

A classical objective in topology optimization of conjugate heat transfer is to maximize heat transfer in the domain without increasing the mechanical pumping power that needs to be spent to overcome friction and move the fluid through the device (nor blocking the fluid flow). This is performed in some studies by maximizing heat transfer under prescribed pressure drop values [22,25], and in others by minimizing pressure drop under prescribed heat transfer performance [39]. As further explained in Section 6, we rather use here multi-criteria optimization and minimize the linear weighted sum of a hydraulic cost function J_v associated with dissipation (to minimize) and a thermal cost function J_Θ measuring the heat transfer efficiency (to maximize, the minimization applies to $-J_\Theta$). This yields

$$J = (1 - \omega) J_v - \omega J_\Theta, \tag{11}$$

where $\omega \in [0;1]$ is the so-called thermal weigh, a measure of the priority given to each objective function ($\omega = 0$ in the pure hydraulic limit, and $\omega = 1$ in the pure thermal limit). Because there does not generally exist a single point minimizing both criteria all together, the solution to such a problem thus aims at identifying the Pareto front [40]. This is the subset of designs that best manage trade-offs between conflicting objectives, in the sense that further pushing the optimization of one objective function will decrease the performance of the other one. Ultimately, a final design is selected from the Pareto optimal subset by a human decision maker based on subjective preferences.

3. Numerical Methods

A pseudo-code outlining the basic procedure for solving the aforementioned topology optimization problem is presented in Algorithm 1, to iterate until either a maximum number of iterations is reached or a user defined convergence tolerance is attained. In essence, this involves employing a finite element immersed numerical framework that integrates the implicit representation of different domains, level set characterization of the interface, and anisotropic remeshing capabilities. For clarity, we discuss separately in subsequent sections the mesh adaptation algorithm and its implementation in a parallel-computing environment, whose applications in the realm of coupled thermal–fluid topology optimization constitute the primary novelty of this study. Throughout the remainder of this section, we delve into each of the other individual steps, examining the associated challenges and the numerical techniques utilized to address them.

Algorithm 1 Design update scheme.

- 1: **loop**
 - 2: Solve the state variables
 - 3: Solve the adjoint variables
 - 4: Solve the gradient of the objective function
 - 5: Displace the interface along the direction of the steepest slope
 - 6: Build a computational anisotropic mesh adapted to the interface position
-

3.1. Variational Multi-Scale Modeling

Equal-order linear approximations for both the velocity and pressure unknowns are used to solve all equations (state, adjoint, level set). This scheme is highly advantageous in the context of the large-scale, three-dimensional applications under consideration due to its straightforward implementation and manageable computational cost. To this end, we utilize stabilized weak forms formulated within the variational multi-scale (VMS) framework. This improves the stability of the Galerkin method by incorporating additional integrals over the element interior, and avoids the spurious node-to-node oscillations classically encountered with discretization schemes violating the Babuska–Brezzi condition. The fundamental concept involves segregating all quantities into coarse- and fine-scale components, representing different resolution levels. Only the large scale is resolved by the finite element mesh, with the effect of the unresolved fine scale onto the large scale modeled after consistently derived residual-based terms; see Appendix B for provision of the various problems tackled by this method, along with additional insights on the use of implicit and explicit discretization schemes.

3.2. Immersed Volume Method

The monolithic immersed volume method (IVM) compounds the solid and fluid phases into a hybrid fluid with variable material properties. This is a key feature for the thermal coupling problems addressed in this study, as the heat exchanged at the interface is solely determined by the individual conductivities and specific heats prescribed on either side, obviating the need to estimate heat transfer coefficients. In essence, this entails solving the state Equations (2)–(4) and adjoint Equations (7)–(9) on a mesh of the entire domain Ω , wherein the fluid domain Ω_f and solid domain Ω_s are immersed, with the interface between these two distinct domains being localized and represented by the level set method. More details about the mathematical formulation within the context of variational multiscale finite element methods can be found in [41,42]. As further elaborated in Section 4, the level set function (1) is used as an anisotropic mesh adaptation criterion which ensures the accurate and smooth distribution of individual material properties over the narrowest possible thickness around the interface. This is typically achieved by linearly interpolating between fluid and solid values, using a transition region with a thickness of a few elements around the interface and a smooth Heaviside function computed from the level set to mitigate discontinuities.

In practice, we compute the composite thermal conductivity as the harmonic mean of the solid and fluid values, i.e.,

$$\frac{1}{k} = \frac{1}{k_f} H_\epsilon(\varphi) + \frac{1}{k_s} (1 - H_\epsilon(\varphi)), \tag{12}$$

where we have noted H_ϵ , the smoothed Heaviside function on Ω_f defined as

$$H_\epsilon(\varphi) = \begin{cases} 1 & \text{if } \varphi < -\epsilon, \\ \frac{1}{2} \left(1 - \frac{\varphi}{\epsilon} - \frac{1}{\pi} \sin\left(\pi \frac{\varphi}{\epsilon}\right) \right) & \text{if } |\varphi| \leq \epsilon, \\ 0 & \text{if } \varphi > \epsilon, \end{cases} \tag{13}$$

and the regularization parameter ϵ is set to twice the mesh size h_\perp in the direction normal to the interface ($\epsilon = 2h_\perp$). This guarantees that the heat flux across the interface is continuous as derived from a steady, one-dimensional analysis of heat flux with no sources, considering stepwise variations in conductivity from one medium to another. For a comprehensive derivation and analysis, refer to [43], and for evidence of the improved numerical accuracy compared to the classical arithmetic mean model, see [44]. The remaining material properties of density, dynamic viscosity, and thermal heat capacity are constant and equivalent to the fluid values, and we enforce zero velocity at all mesh nodes within the solid domain. Compared to utilizing extremely high ratios of solid-to-fluid viscosity to ensure zero deformation in Ω_s , the present approach serves as a stringent constraint that efficiently prevents fluid leakage across the immersed interface, which is because anisotropic mesh adaptation ensures that the interface does not intersect the mesh elements arbitrarily but instead aligns the mesh element edges precisely along the interface, thereby preserving the accuracy of the finite element approach.

3.3. Interface Update Scheme

At each step, the level set is evolved by solving a transport equation with normal velocity of $\beta \mathbf{n} / \Delta \tau$, where β is a displacement in the direction of the steepest descent computed from the sensitivity analysis, and $\Delta \tau$ represents a pseudo-time step for converting from displacement to velocity. It is worth noting that this pseudo-time step has no physical significance, as our concern is solely with the relative displacement of a given point on the interface with respect to its neighbors, not its absolute displacement. This transport equation can be formulated over the entire (solid–fluid) domain since the vector normal to the interface $\mathbf{n} = \nabla \varphi / \|\nabla \varphi\|$ can be computed in Ω using (1). A major challenge, however, arises with this approach, as the level set is often no longer a distance function after transport. This poses significant issues for the purpose of performing anisotropic mesh adaptation, given that the intended remeshing strategy relies on the distance property at the interface. Consequently, a coupled convection–reinitialization method is used to recover this feature by automatically reinitializing the level set function during the resolution of the transport equation. In practice, the signed distance function is truncated using a hyperbolic tangent filter as given by the following equation.

$$\phi = E \tanh\left(\frac{\varphi}{E}\right), \tag{14}$$

where E is the so-called cut-off thickness ensuring that the metric property is appropriately, asymptotically fulfilled near the zero iso-value. In order to evolve this filtered level set, the following auto-reinitialization equation is solved:

$$\partial_\tau \phi + \mathbf{a}_\tau \cdot \nabla \phi = S, \tag{15}$$

where

$$\mathbf{a}_\tau = \frac{\beta}{\Delta\tau} \mathbf{n} + \frac{\lambda}{\Delta\tau} \operatorname{sgn}(\phi) \frac{\nabla\phi}{\|\nabla\phi\|}, \quad S = \frac{\lambda}{\Delta\tau} \operatorname{sgn}(\phi) \left(1 - \left(\frac{\phi}{E} \right)^2 \right), \quad (16)$$

where λ represents a parameter with units of length, chosen to be equal to h_\perp . As demonstrated in [45–47], this approach ensures faster resolution and better mass conservation compared to the classical Hamilton–Jacobi method, where both steps are performed successively. Another advantage lies in the fact that because the filtered level set defined in (14) is bounded, Dirichlet boundary conditions can be easily appended to Equation (15) to specify which sub-regions of $\partial\Omega$ are fluids and which ones are solid. In practice, we set $\phi = -E$ (fluid) at the inlet and outlet, and $\phi = E$ (solid) everywhere else.

4. Anisotropic Mesh Adaptation

4.1. Construction of an Anisotropic Mesh

The fundamental concept behind anisotropic, metric-based mesh adaptation is to build a mesh that should be isotropic with uniform elements in a designated Riemannian space but anisotropic with elongated adapted elements in the canonical Euclidean space. Assuming that controlling the interpolation error adequately manages the overall approximation error in the context of metric-based adaptation methods, the problem objective is to determine the mesh, consisting of, at most, N_n nodes, that minimizes the interpolation error in the L^1 norm. Following the approach outlined in [48,49], this is performed by combining an edge-based error estimator and a gradient recovery procedure to compute a metric tensor providing a set of anisotropic directions and stretching factors of mesh elements along these directions directly at the nodes, without any direct input from the mesh elements or any interpolation. The stretching factor field is determined by solving an optimization problem based on the equi-distribution principle while adhering to the constraint of a fixed number of mesh nodes. Finally, a new mesh is built, following the layout reported in [50], that relies on a topological representation of the computational domain.

4.2. Edge Error Estimate

Let Ω_h represent a mesh of the domain Ω , and, considering a regular, analytical, scalar function ψ defined on Ω , let ψ_h represent its linear finite element approximation on Ω_h . In what follows, we denote by $\Sigma(i)$ the set of nodes connected to a given node \mathbf{x}^i in Ω_h , by $|\Sigma(i)|$ the number of such nodes, and by \mathbf{x}^{ij} the edge connecting \mathbf{x}^i to another node $\mathbf{x}^j \in \Sigma(i)$. Following the methodology outlined in [48], we estimate the interpolation error along \mathbf{x}^{ij} by projecting the second derivative of ψ along the edge. This is achieved by projecting a Taylor expansion of the gradient of ψ at \mathbf{x}^j along the edge, resulting in

$$\varepsilon_{ij} = |\mathbf{g}^{ij} \cdot \mathbf{x}^{ij}|. \quad (17)$$

Here, a superscript i (respectively, j) indicates a nodal value at \mathbf{x}^i (respectively, \mathbf{x}^j). Also, we denote by $\mathbf{g}^i = \nabla\psi(\mathbf{x}^i)$ and $\mathbf{g}^{ij} = \mathbf{g}^j - \mathbf{g}^i$ the exact value of the gradient of ψ at \mathbf{x}^i , and the variation of this gradient along the edge. In theory, Equation (17) can be computed without resource-intensive Hessian reconstruction techniques, as it involves only gradient values at the edge extremities. Nonetheless, it still necessitates the gradient of ψ to be known and continuous at the nodes. This, in turn, requires complete knowledge of ψ , while in practice, only the finite element approximation ψ_h is available, whose gradient is piecewise constant (since the approximation is linear) and discontinuous from one element to another (unlike its projection along the edges, that depends solely on the nodal values of the field, and thus remains continuous).

Consequently, a gradient recovery technique is employed to provide a continuous gradient estimator directly at the nodes. It has been demonstrated in [48] that by replacing the

reconstructed gradient with the exact gradient in (17), a suitable error estimate preserving second-order accuracy is achieved. This yields

$$\varepsilon_{ij} = |\bar{\mathbf{g}}^{ij} \cdot \mathbf{x}^{ij}|, \tag{18}$$

where we note $\bar{\mathbf{g}}^i$ as the recovered gradient of ψ_h at node \mathbf{x}^i , and $\bar{\mathbf{g}}^{ij} = \bar{\mathbf{g}}^j - \bar{\mathbf{g}}^i$. The best approximate solution in terms of least squares utilizing only the nodal values as input is demonstrated in [48] to be

$$\bar{\mathbf{g}}^i = (\mathbf{X}^i)^{-1} \cdot \sum_{j \in \Sigma(i)} (\psi_h(\mathbf{x}^j) - \psi_h(\mathbf{x}^i)) \mathbf{x}^{ij}, \tag{19}$$

where we have introduced the length distribution tensor \mathbf{X}^i defined as

$$\mathbf{X}^i = \frac{1}{|\Sigma(i)|} \sum_{j \in \Sigma(i)} \mathbf{x}^{ij} \otimes \mathbf{x}^{ij}, \tag{20}$$

to provide an average representation of the distribution of edges sharing an extremity.

4.3. Metric Construction

At this stage, the stretching factor s_{ij} defined as the ratio between the length of \mathbf{x}^{ij} after and before adaptation is introduced to bind the error indicator ε_{ij} defined in (18) and a metric suitable for mesh adaptation. The metric at node \mathbf{x}^i is intended to result in a unit stretched edge length in the metric space as expressed by

$$(s_{ij} \mathbf{x}^{ij})^T \cdot \mathbf{M}^i \cdot (s_{ij} \mathbf{x}^{ij}) = 1, \quad \forall j \in \Sigma(i), \tag{21}$$

for which an approximate solution in terms of least squares is demonstrated in [48] to be

$$\mathbf{M}^i = \left(\frac{d}{|\Sigma(i)|} \sum_{j \in \Sigma(i)} s_{ij}^2 \mathbf{x}^{ij} \otimes \mathbf{x}^{ij} \right)^{-1}, \tag{22}$$

assuming the nodes in $\Sigma(i)$ form at least d non-collinear edges with \mathbf{x}^i (which holds true for a valid mesh). Ultimately, the solution to (22) is determined by prescribing a target number of nodes N_n . Provided the total error is equally distributed among all edges, it is shown in [49] that the stretching factor is given by

$$s_{ij} = \left(\frac{1}{N_n} \sum_i N_i \right)^{\frac{2}{d}} \varepsilon_{ij}^{-1/2}, \tag{23}$$

where the number of nodes N_i generated for a unit error in the vicinity of \mathbf{x}^i is such that

$$\frac{1}{N_i^2} = \det \left(\frac{d}{|\Sigma(i)|} \sum_{j \in \Sigma(i)} \varepsilon_{ij}^{1/2} \frac{\mathbf{x}^{ij}}{|\mathbf{x}^{ij}|} \otimes \frac{\mathbf{x}^{ij}}{|\mathbf{x}^{ij}|} \right). \tag{24}$$

4.4. Level Set-Based Adaptation Criteria

To streamline the presentation, Algorithm 2 summarizes the key steps required for nodal metric construction. In practice, only the filtered level set defined in (14) is used for error estimation purposes, as it preserves the zero iso-value of ϕ and fulfills the metric property in a thin layer around the interface. This allows to convey the relevant information while avoiding unnecessary mesh adaptation away from the interface, where the interpolation error is minimal since $\|\nabla \phi\| \sim 0$. In return, the mesh adaptation criterion is purely geometric, meaning that the mesh can be adapted beforehand and then utilized to compute all numerical solutions (state, adjoint) involved in the subsequent design update step.

Algorithm 2 Anisotropic mesh adaptation algorithm.

Require: Initial mesh and associated P1 finite element approximation

- 1: Set target number of nodes N_n
 - 2: **for** each node \mathbf{x}^i **do**
 - 3: Compute the nodal recovered gradient $\bar{\mathbf{g}}^i$ using (19)–(20)
 - 4: **for** each edge \mathbf{x}^{ij} **do**
 - 5: Compute the stretching factor s_{ij} using (23) (requires computing the recovered gradient $\bar{\mathbf{g}}^{ij} = \bar{\mathbf{g}}^j - \bar{\mathbf{g}}^i$ and the edge-based error ε_{ij} using (18))
 - 6: Compute metric \mathbf{M}^i using (22)
 - 7: Update the current mesh by local improvement in the neighborhood of the nodes and edges [50]
 - 8: Perform linear interpolation of ψ_h on the updated mesh
-

However, it is important to note that the same approach can accommodate more intricate physically informed adaptation criteria for dynamic mesh adaptation during simulations. This would classically require using a metric intersection algorithm to combine the various metrics associated with each individual adaptation criterion. However, the relatively high computational cost of such methods, as well as their disposition to lead to non-unique, suboptimal outcomes, is often raised as a major limitation. In contrast, the present approach enables the construction of a unique metric directly from a multi-component error vector combining all quantities (level set, flow) of interest. For instance, if we consider a vector $\boldsymbol{\psi} = (\psi_1, \psi_2, \dots, \psi_p)$ consisting of p scalar variables, the L-2 norm of the error vector $\boldsymbol{\varepsilon}_{ij} = (\varepsilon_{ij}, 1, \varepsilon_{ij,2}, \dots, \varepsilon_{ij,p})$ can serve as a simple (scalar) error value from which the stretching factors and, ultimately, the metric tensor can be computed. For instance, a $2d + 5$ sized nodal vector field

$$\boldsymbol{\psi}_h(\mathbf{x}^i) = \left(\frac{\phi_h^i}{\max_{j \in \Sigma(i)} \phi_h^j}, \frac{u_{h_{k \in \{1 \dots d\}}}^i}{\|\mathbf{u}_h^i\|}, \frac{\|\mathbf{u}_h^i\|}{\max_{j \in \Sigma(i)} \|\mathbf{u}_h^j\|}, \frac{T_h^i}{\max_{j \in \Sigma(i)} T_h^j}, \frac{\tilde{u}_{h_{k \in \{1 \dots d\}}}^i}{\|\tilde{\mathbf{u}}_h^i\|}, \frac{\|\tilde{\mathbf{u}}_h^i\|}{\max_{j \in \Sigma(i)} \|\tilde{\mathbf{u}}_h^j\|}, \frac{\tilde{T}_h^i}{\max_{j \in \Sigma(i)} \tilde{T}_h^j} \right), \quad (25)$$

allows to perform mesh adaptation with respect to (besides the level set) the state and adjoint temperatures, as well as the state and adjoint velocities, in norm and direction. Note, all fields here are normalized by their global maximum, which prevents any field with a significantly larger magnitude to dominate the error estimator, and ensures that variations in all variables are fairly balanced. This is expected to be especially relevant in the context of fluid flow topology optimization, as it can help encompass the conflicting demand of high-accuracy state and adjoint approximations, as those have very different spatial supports in convection-dominated problems (because the linearized evolution operator is non-normal [51]).

5. Numerical Implementation Details

5.1. Enforcing Geometric Constraints

Most fluid flow topology optimization problems must be solved under user-defined geometrical constraints meant to prevent far-fetched optimal layouts, where the solid domain either vanishes entirely (for instance, to minimize drag) or entirely obstructs the design space (for instance, to minimize a pressure drop). Constant or upper-bounded surfaces and/or volumes are topical examples for which the classical approach is to add penalty terms to the Lagrangian. Each penalty term is formulated as the product of a degree of constraint violation and an empirical penalty parameter, and affects the derivation of the sensitivity function through its variations with respect to both state and design variables. This study rather enforces a constant volume of fluid constraint $V = V_{target}$ in an a posteriori manner. In other words, the problem described in Section 2 is solved without any constraint, although the optimization still adheres to the coupled Navier–Stokes and heat equations as

state equations. After evolving the interface position with the convective level set method presented in Appendix B.5, an initial pass of anisotropic mesh adaptation occurs, followed by the computation of the fluid domain volume. The latter is expressed as

$$V_\varphi = \int_{\Omega} H_\epsilon(\varphi) \, dv, \tag{26}$$

where H_ϵ is the Heaviside function defined in (13). Then, a constant deformation $\delta\varphi$ whose effect is either to expand (if negative) or contract (if positive) the fluid domain is optimized by a straightforward dichotomy algorithm. Once the distance $|V_{\varphi+\delta\varphi} - V_{target}|$ between the current and target volumes falls under a specified tolerance, the optimally deformed level set is truncated and another pass of mesh adaptation occurs. Two notable features should be emphasized: firstly, only small deformations are applied. This obviates the need for in-between mesh adaptation iterations, and guarantees that the numerical cost of enforcing the volume of fluid constraint is primarily determined by the second pass of mesh adaptation. Secondly, the level set function φ must be available for the aforementioned strategy to be tractable (not only its filtered counterpart ϕ , whose maximum and minimum values are altered by each offset). Given that only the filtered level set (not the level set itself) is updated during the convection–reinitialization step, this is achieved using a brute force algorithm to entirely reconstruct the distance beforehand from the zero iso-value of ϕ .

5.2. Gradient Descent Optimization

In practice, the update step uses the displacement

$$\beta = -\theta \frac{\beta_0 \chi_\Gamma(\mathbf{x})}{\max_{\Omega} \beta_0 \chi_\Gamma(\mathbf{x}) \prod_l \zeta(\|\mathbf{x} - \mathbf{x}_s^l\|)}, \tag{27}$$

where β_0 is the steepest descent estimate estimated from (10), and the parameter $\theta > 0$ serves as a descent factor that regulates the size of the step taken in the steepest descent direction. Meanwhile, χ_Γ and ζ denote activation functions constrained within the range of 0 to 1, whose role is to guarantee that updates to the design occur only within appropriate regions of the computational domain. Further elaboration is provided below:

- The function χ_Γ serves as a binary filter, yielding a value of 1 solely at nodes located within a distance E from the interface. The rationale for doing so is that $\|\nabla\phi\|$ only tends asymptotically to zero. Consequently, the normal vector $\mathbf{n} = \nabla\phi/\|\nabla\phi\|$ maintains a unit norm and the displacement maintains a non-zero value across the entire fluid domain, even in regions far from the interface, which can result in numerical break down at nodes close to equidistant from two different parts of the interfaces (such as the centerline of a channel).
- On the other hand, the function ζ acts as a smooth filter that assigns a value of 0 to certain subsets (either a point or a curve) $\mathbf{x}_s^l \in \partial\Omega$. Said subsets are selected prior to optimization by a human decision maker as those regions of the computational domain where poorly defined velocity gradients are susceptible to trigger large but non-physical displacements. Such singular points (e.g., sharp edges and corner points) are best removed manually from the normalization step to prevent a substantial slowdown in the convergence rate of the optimization, as they would yield excessively small displacements along the remaining interface. In this context, we use hyperbolic tangent filters defined as

$$\zeta(r) = \frac{1}{2} + \frac{1}{2} \tanh\left(\alpha \tan\left(-\frac{\pi}{2} + \frac{\pi}{2} \frac{r}{r_s + \epsilon_1} + \epsilon_2\right)\right), \tag{28}$$

where we denote by $r = \|\mathbf{x} - \mathbf{x}_s^l\|$ the shortest path distance to the singularity, the parameter α governs the steepness of the transition, while $\epsilon_{1,2}$ are small regularization

parameters utilized to mitigate local discontinuities. Additionally, r_s is a transition radius set such that

$$4r_s < \min_{l,m} \|\mathbf{x}_s^l - \mathbf{x}_s^m\|, \quad (29)$$

to ensure that a value of 1 is assigned to all nodes in between two adjacent singularities.

In conclusion, the filtering and normalization procedures described above guarantee that the level set update step relies on a displacement that is nonzero only within a narrow layer with a thickness of E around the interface, except for a specified number of pre-selected singular subsets.

5.3. Step Size

In practical application, the displacement within the designated update region (that can be computed as the difference between the zero iso-value of the filtered level set before and after evolving the interface) is significantly smaller than its theoretical value given by the descent factor θ . This phenomenon arises because the state and adjoint velocities within the solid domain are both zero. It follows that the displacement (driven by the gradient of these velocity fields) is also zero across the entirety of the solid, except in the near vicinity of the interface, and that an explicit control over the numerical displacement achieved at each iteration is unattainable. One conceivable approach to overcome this issue would involve iteratively evolving the interface with a small descent factor until the disparity between the accumulated displacement and the target value falls below a specified tolerance threshold. However, the interface can only be evolved once per update step, as the gradient information becomes irretrievable if the solid happens to shrink (for the same aforementioned reason). Hence, the step size is manually adjusted on a case-by-case basis to ensure that the achieved displacement is marginally less than the prescribed cut-off thickness. This approach strikes a balance between accuracy and computational efficiency, as it keeps the number of iterations necessary for convergence within reasonable bounds while accurately tracking the position of the evolved interface. Conversely, displacements exceeding the cut-off thickness tend to relocate the level set into regions of the computational domain lacking adequate mesh refinement, ultimately compromising the accuracy of the interface representation.

5.4. Parallel Resolution

The physical problems addressed in this study (e.g., state and adjoint Navier–Stokes equations, state and adjoint heat equations, and level set transport) call for the efficient computation, storage, and resolution of large-scale linear systems. In this regard, a given finite element formulation is sequentially implemented at the element level. All local contributions are then assembled, and the full-scale system is solved in parallel utilizing the PETSc library [52], whose broad array of parallel data structures, including linear and non-linear solvers and preconditioners, scales to large computing architectures. In this work, only semi-implicit and explicit discretization schemes are utilized (see Appendix B), meaning that only one linear system is solved per temporal iteration, with sufficient conditioning to be amenable to iterative methods. Consequently, we employ the Generalized Minimal Residual (GMRES) algorithm with block Jacobi incomplete LU preconditioning, deeming the solutions converged when the absolute residuals fall below 10^{-6} .

5.5. General Algorithm

Figure 1 illustrates the flowchart outlining the developed topology optimization algorithm. The parameters essential to all examples discussed subsequently are provided in Table 1. It is worth noting that we iterate until a maximum number of iterations is reached and assess convergence subsequently. This is because, due to the level set-based technique utilized for the purpose of enforcing the volume of fluid constraint, convergence

is attained when the displacement is uniform (not zero) along the interface, which is not easily surveyed dynamically.

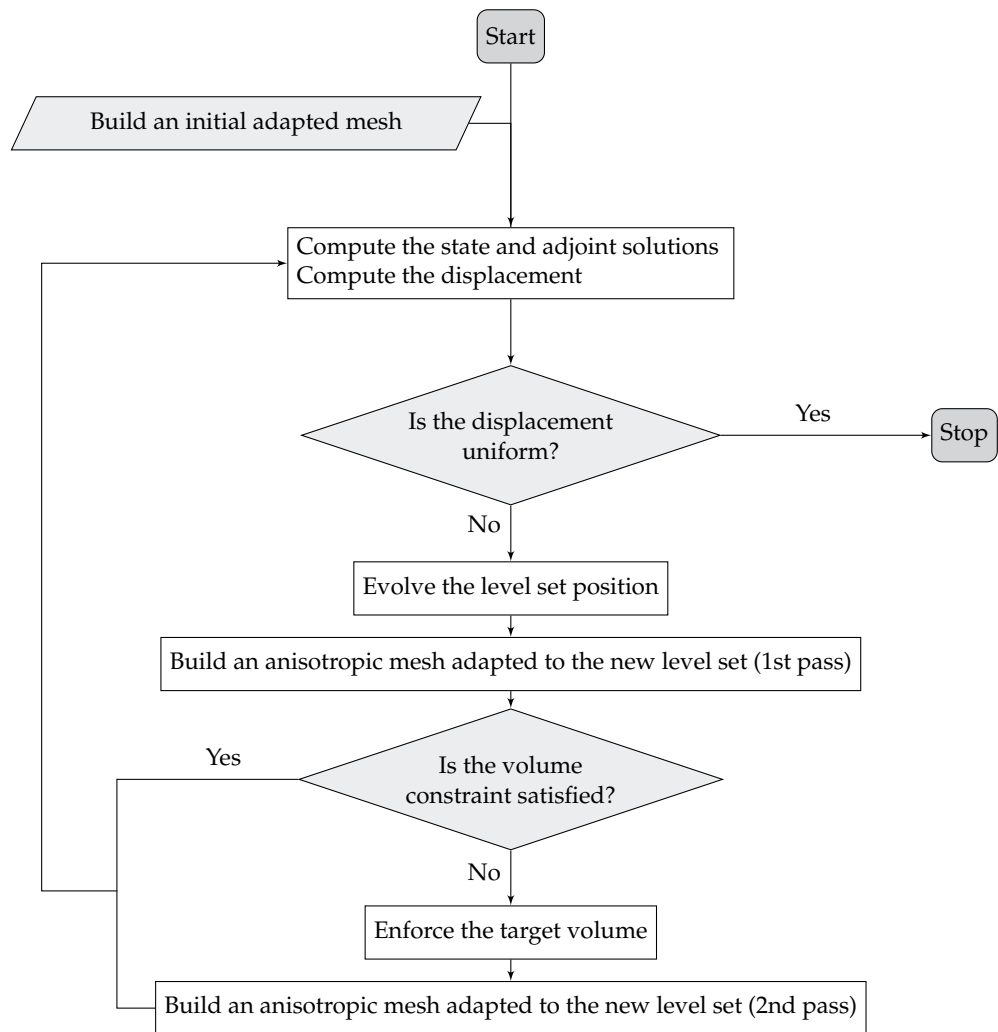


Figure 1. Flowchart depicting the procedure for performance-based topology optimization.

Table 1. Algorithmic parameters.

$h_{\perp} = 0.0001$	Minimum mesh size normal to the interface
$\Delta t = 0.1$	CFD time step
$E = 0.005$	Thickness for level set truncation
$ \delta\varphi = [0.0005; 0.001]$	Initial offset for volume recovery
$r_s = 0.0125$	Transition radius
$\alpha = 2.1$	Sharpness parameter
$(\epsilon_1, \epsilon_2) = (0.0005, 0.005)$	Regularization parameters

6. Numerical Benchmarks

6.1. Preliminaries

In this section, a series of topology optimization problems are tackled to demonstrate the effectiveness of the numerical framework and illustrate the accuracy with which the interfaces of the computed layouts are captured within the simulation models. We consider various cases in both 2-D and 3-D settings, with the objective of minimizing the pressure drop through the network of fluid channels while simultaneously maximizing heat transfer within the domain. For this purpose, we solve a bi-objective optimization problem and minimize the linear weighted sum (11) of two cost functions: a hydraulic cost function

J_v to quantify the net inward flux of total pressure through the inlet and outlet boundary conditions (to be minimized [36]), and a thermal cost function J_Θ to quantify the recoverable thermal power (to be maximized [53]). Keeping in mind that the orientation of the normal vector yields positive (respectively, negative) values of $\mathbf{u} \cdot \mathbf{n}$ at the inlet (respectively, at the outlet), the above cost functions are expressed in the form of (5) according to

$$J_v = p_{tot}(\mathbf{u} \cdot \mathbf{n}) = \left(p + \frac{1}{2}\rho(\mathbf{u} \cdot \mathbf{u})\right)(\mathbf{u} \cdot \mathbf{n}), \quad \text{and} \quad J_\Theta = \rho c_p T(\mathbf{u} \cdot \mathbf{n}). \quad (30)$$

In all cases, a reference design domain is chosen under the form of a cubic or cuboid (parallelepipedic) cavity, with a cylindrical inlet and outlet at which parabolic normal velocities are prescribed as defined by

$$\mathbf{u}_{i,o} = u_{i,o} \left(1 - \frac{4r^2}{e_{i,o}^2}\right) \mathbf{n}, \quad (31)$$

where r represents the distance to the center of the inlet/outlet, $e_{i,o}$ are the inlet and outlet diameters, $u_{i,o}$ are the inlet/outlet centerline velocities, adjusted so that the same mass flows enter through the inlet and exit through the outlet. In each case, the control parameters consist of the Prandtl number and the Reynolds number (for which the inlet diameter and the maximum inlet velocity are used as reference scales).

Here are the remaining practical implementation details:

- Initially, all design domains are populated with solid inclusions of diverse sizes and shapes. Based on prior experience, the problems addressed herein are largely insensitive to the initial design as long as an ample number of inclusions is utilized. We keep in mind that additional techniques for the seeding of new solid inclusions could be integrated into the proposed framework, but such enhancements are beyond the scope of this study.
- The permissible error margin on the target volume is 1% in 2-D settings, and 5% in 3-D settings.
- The fluid enters and exits the design domain through leads extending normal to the boundary, whose length $l_{i,o}$ is uniform across all inlets and outlets. This practice ensures numerical consistency, as the precise problem formulation in the literature can differ from one study to another, without it being clear whether such leads are encompassed within the design domain. This is true in the present case, although the leads are not factored into the volume constraint, the definition of the target volume, or the computation of the volume of fluid.
- The sharp intersections between the leads and the cavity boundaries make for the singular subsets to be excluded from the displacement normalization step. Given that all inlets and outlets are cylindrical in shape, all ζ filters needed to compute the actual displacement increase from 0 to 1 over either a circle of radius $2r_s$ (in a 2-D setting) or a torus with a minor radius of $2r_s$ and a major radius equal to the inlet/outlet radius (in a 3-D setting).
- In order to factor out the leads from the displacement normalization procedure and prevent a slowdown in the optimization convergence rate, a binary filter assigning a value of 0 to all nodes within the leads is added to the max argument of (27). Without this modification, the maximum displacement would occur in the leads, as the most straightforward method to minimize the pressure loss is to obstruct flow by completely blocking the leads with solid material.
- While not specifically aimed at optimizing performance, all optimization runs have been observed to converge within a few hundred iterations. As detailed further ahead, this convergence typically corresponds to the number of steps required to satisfy the fluid volume constraint while ensuring that the displacement at each iteration does not exceed the prescribed level set cut-off thickness.

- As expected for dense meshes composed of tetrahedral/triangular elements, we have checked the element-to-node ratios of all meshes to be close to five (in 3-D settings, two in 2-D settings), which is expected for dense meshes composed of tetrahedral/triangular elements. In what follows, we align on existing literature by reporting the mesh information in terms of the equivalent number of elements, hence $N_{el} = 5N_n$ (in 3-D, $N_{el} = 2N_n$ in 2-D).
- The number of mesh elements remains constant throughout the optimization procedure to ensure a consistent evaluation of the numerical cost (see Section 7) although the implementation does allow to adjust the mesh refinement as needed.

6.2. Two-Dimensional Splitter Device with Two Outlets

To initially verify and characterize the method, we focus first on a purely hydraulic ($\omega = 0$) problem aiming at minimizing power dissipation in a 2-D flow splitter device, a classical example of a functional unit used for the continuous separation and collection of particles in microchannels [54], and a class of flow that has received attention as a relevant example of topology optimization in fluid dynamics [55,56]. The design domain sketched in Figure 2 is a square cavity of unit height, with a single inlet at the bottom and two outlets at the left size on the left and right sides. The objective is to identify the optimal layout for connecting the inlet to the outlets, while ensuring that the fluid occupies 20% of the cavity and that the flow is evenly distributed among all outlet orifices (so, each outlet is to receive half of the fluid flow entering through the inlet). The remaining problem parameters are provided in Table 2. The initial design depicted in Figure 3 comprises spherical occlusions arranged to fill approximately 50% of the cavity, thereby violating the volume constraint. This occurs because a larger number of smaller inclusions are required to attain the correct volume, which would either substantially increase the number of mesh elements required to maintain numerical accuracy (due to the increased interfacial surface area) or risk obstructing the fluid domain due to inadequate mesh refinement. In return, the convergence history plot in Figure 4 shows that the cost function is initially low despite carrying little physical significance. This transient phase continues until the volume of fluid reaches the target within the desired tolerance, at which point the cost function adjusts accordingly until a feasible minimum is attained.

For this case, 500 iterations have been completed using meshes comprising of 30,000 elements. As can be seen from the samples illustrated in Figure 3, several intricate stages occur during the optimization process that involve multiple canceling and merging of holes, all accurately captured on anisotropic adapted meshes displaying adequate refinement and deformation. Namely, all mesh elements are fine and very elongated near the interface between the solid and fluid, which ensures a smooth transition of velocity to zero across the boundary layer but a coarse and uniform distance from the interface, particularly within the solid where only a few tens of elements are employed. Ultimately, the optimal duct configuration for this scenario comprises a wide pipe splitting midway into two thinner pipes with nearly diameters, each connecting to an outlet. This turns to be a balanced compromise between transporting fluid along the widest possible pipe and along the shortest route, which aligns with the findings in ref. [55]. Importantly, we note that the quality issue affecting solutions in the aforementioned reference (staircasing in smoothly curved regions), are efficiently mitigated by anisotropic mesh adaptation, as we systematically obtain here smooth and sharply delineated interfaces at all optimization stages, including within the leads. Similar trends are noted when evaluating the robustness of the optimal layout to changes in the design parameters, such as the volume of fluid allowed in the layout, or the ratio of flow rate at the outlets. This is evidenced in Figure 5a showing the final ducts optimized for several volume of fluid constraints in a range from 10 to 50%. Overall, the obtained results show that decreasing the volume of fluid simply slims down the optimal channels but increases the dissipated power, which occurs because shear is the main mechanism for energy dissipation at such low Reynolds numbers. Therefore, an ideal flow pipe should ideally be as wide and short as feasible (note, the analysis

overlooks the mass of the layout, which obviously puts a limit on how much fluid should be allowed in a practical device). Similarly, we show in Figure 5b the final ducts optimized for several flow rate ratios ranging from 1:9 (i.e., 10% at the lower outlet vs. 90% at the upper outlet) to 9:1. The results show that the larger the flow rate at a certain outlet, the thicker the channel, which is fully consistent with the previous findings. Ultimately, less power is dissipated if the flow rate is larger at the lower outlet, with the 1:9 optimal being lower than its 9:1 counterpart by 25%. This is simply because a larger flow rate makes for a shorter path between the inlet and the outlet; plus, there is little cost in bending the fluid stream shortly after it enters the domain due to most of the fluid flowing in the inner, shorter region.

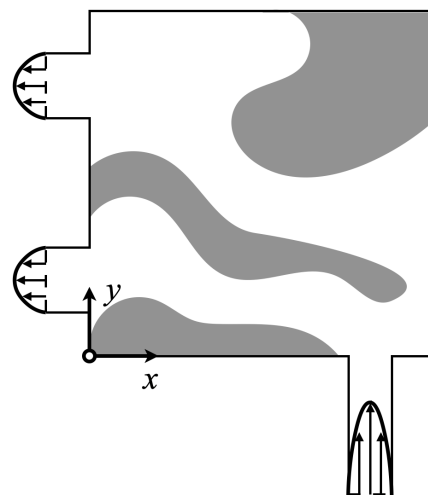


Figure 2. Set-up of the two-dimensional flow splitter problem. The light gray shade denotes the solid layout.

Table 2. Numerical parameters for the two-dimensional flow splitter device problem.

$\Omega = [0; 1] \times [0; 1]$	Design domain
$d = 2$	Problem dimensionality
$V_{target} = 0.25$	Target volume of fluid
$V_{\varphi,0} = 0.50$	Initial volume of fluid
$Re = 2$	Reynolds number
$u_i = 0.3$	Inlet centerline velocity
$e_i = 0.125$	Inlet diameter
$l_i = 0.4$	Inlet leads length
$\mathbf{x}_{i1} = (0.8125, -0.4)$	Inlet center coordinates
$u_{o1} = 0.1$	Outlet 1 centerline velocity
$u_{o2} = 0.1$	Outlet 2 centerline velocity
$e_o = 0.1875$	Outlet diameter
$l_o = 0.125$	Outlet leads length
$\mathbf{x}_{o1} = (-0.125, 0.21875)$	Outlet 1 center coordinates
$\mathbf{x}_{o2} = (-0.125, 0.78125)$	Outlet 2 center coordinates
$N_n = 30,000$	Nb. mesh nodes
$N_{el} = 60,000$	Nb. mesh elements

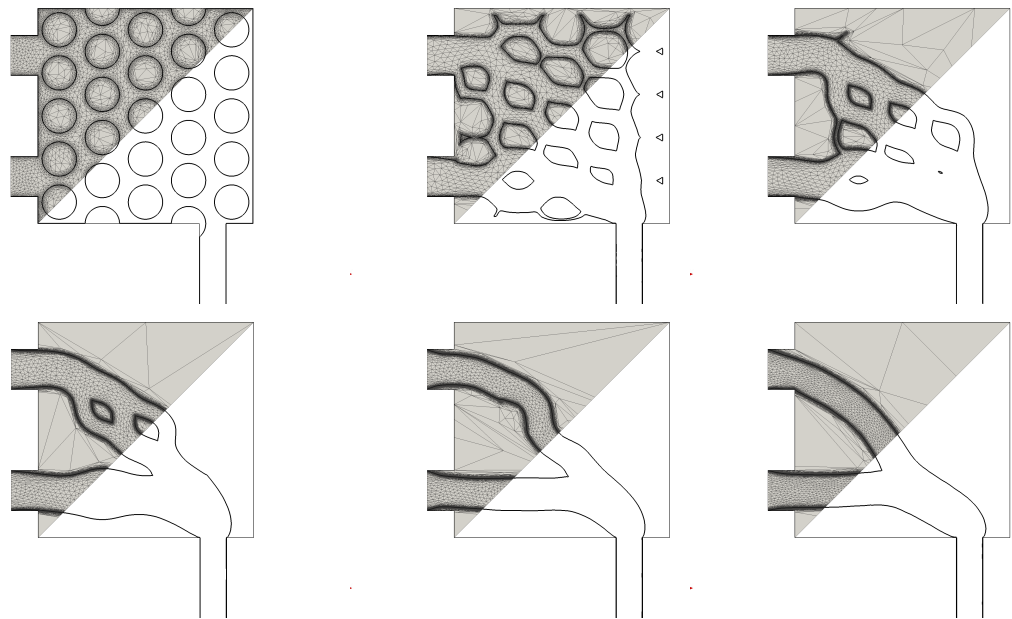


Figure 3. Hydraulic optimization of the two-dimensional flow splitter device presented in Figure 2. From left to right and from top to bottom: the zero iso-value of the level set function and the corresponding anisotropic adapted meshes are sampled throughout the optimization process using the parameters outlined in Table 2. The volume of the fluid domain in each layout is 49.5%, 45.4%, 40.6%, 34.7%, 24.8% and 24.9%, respectively.

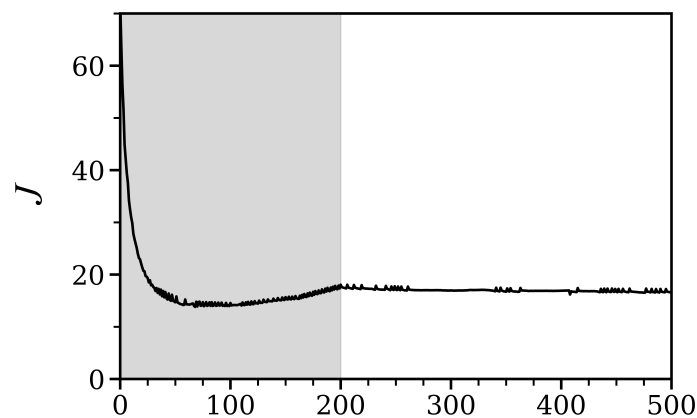


Figure 4. Convergence history for the two-dimensional flow splitter device presented in Figure 2. All cost function evaluations are normalized using the inlet maximum velocity and diameter (or equivalently, using $\rho u_i^3 e_i$ as reference cost functional value). The grey shade indicates the iterations during which the volume constraint is adjusted to its target value.

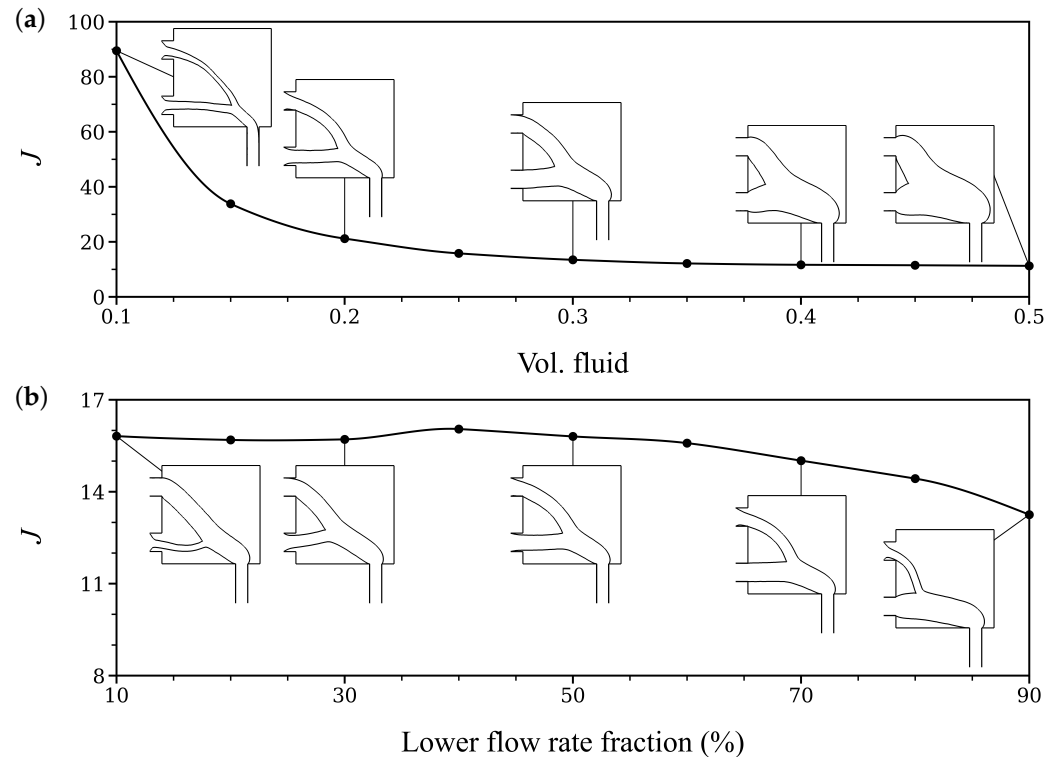


Figure 5. Sensitivity of the optimal design against (a) the volume of fluid allowed in the design domain, and (b) the fraction of fluid leaving the design domain through the lower outlet, for the two-dimensional flow splitter device presented in Figure 2. All cost function evaluations are normalized using the inlet maximum velocity and width (or equivalently, using $\rho u_i^3 e_i$ as reference cost functional value).

6.3. Two-Dimensional Single Pipe with Heated Walls

The second case study is a two-dimensional conjugate heat transfer problem that has received substantial attention in the recent literature [26,32,53,57]. The design domain shown in Figure 6 is a square cavity of unit height. It has a single inlet on the left side and a single outlet on the right side lined up in front of each other, and is discretized with 50,000 mesh elements. A cold fluid is flowing from the inlet, and is heated by the top and bottom walls, subject to a fixed (hot) temperature. All other walls (cavity and leads) are insulated from the surroundings with zero heat absorbed or released (i.e., adiabatic). The solid is set to be 10 times more diffusive than the fluid, which allows using fluid to insulate thermally inner regions from the cold inlet temperature. The aim is to determine the optimal design that connects the inlet to the outlets subject to the constraint that the fluid must occupy 40% percent of the cavity (twice as much as the straight parallel pipe fitting exactly to the inlet and outlet). All other problem parameters, including Reynolds and Prandtl numbers, are given in Table 3. Note, because the inlet and outlet diameters are the same, mass conservation demands the same velocity condition to be prescribed at the inlet and outlet. We do not share the view expressed in [26] that this is ill-posed, in the sense that it does force the algorithm to identify acceptable trade-offs between both hydraulic and thermal for heat and mass transfer optimization without yielding broken flow paths, dead ends or non-physical artifacts, which is the desired goal. Moreover, the argument that the optimization is limited by the fact that the sole variables left to optimization are the pressure (not total pressure) drop between the inlet and outlet, and the outlet temperature (which removes the need to explore, e.g., converging or narrowing channels designs aimed at increasing the fluid velocity), while true in this particular setting, does not hold if multiple inlets/outlets or different inlet/outlet diameters are used.

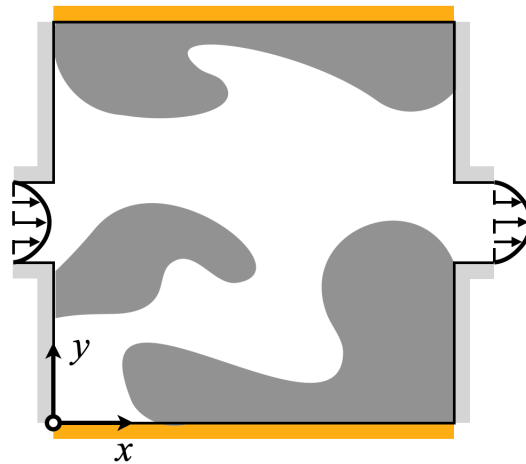


Figure 6. Set-up of the two-dimensional single-pipe problem with heated walls. The orange and light gray shades denote hot isothermal and adiabatic walls, respectively.

Table 3. Numerical parameters for the two-dimensional single-pipe problem with heated walls.

$\Omega = [0;1] \times [0;1]$	Design domain
$d = 2$	Problem dimensionality
$V_{target} = 0.4$	Target volume of fluid
$V_{\varphi,0} = 0.4$	Initial volume of fluid
$Re = 4.5$	Reynolds number
$Pr = 5$	Prandtl number (fluid)
$k_s/k_f = 10$	Solid to fluid thermal diffusivity ratio
$T_w = 10$	Hot wall temperature
$u_i = 1$	Inlet centerline velocity
$T_i = 0$	Inlet cold temperature
$e = 0.2$	Inlet diameter
$l_i = 0.1$	Inlet leads length
$\mathbf{x}_i = (-0.1, 0.5)$	Inlet center coordinates
$u_o = 1$	Outlet centerline velocity
$e_o = 0.2$	Outlet diameter
$l_o = 0.1$	Outlet lead length
$\mathbf{x}_o = (1.1, 0.5)$	Outlet 1 center coordinates
$N_n = 25,000$	Nb. mesh nodes
$N_{el} = 50,000$	Nb. mesh elements

We show in Figure 7 distinct optimal designs computed by progressively increasing the thermal weight, to which we refer below for further discussion. It is important to note that all optimization runs again undergo several heterogeneous stages, all precisely captured on anisotropic adapted meshes comprised of highly stretched elements on either side of the interface. This is evidenced by the selected samples shown in Figures 8 and 9, where the main difference compared to the hydraulic case in Section 6.2 is the finer element size used to discretize the inner solid domain (here the same as in the inner fluid domain) to accurately resolve heat conduction. This is all the more important given that the increased non-linearity of the optimization problem at large thermal weights (where there is almost no contribution from the hydraulic cost function) yields strongly anisotropic material distributions that require adequately capturing the formation and destruction of very fine cross-flow fluid structures whose diameter can be below 1/20 the inlet diameter.

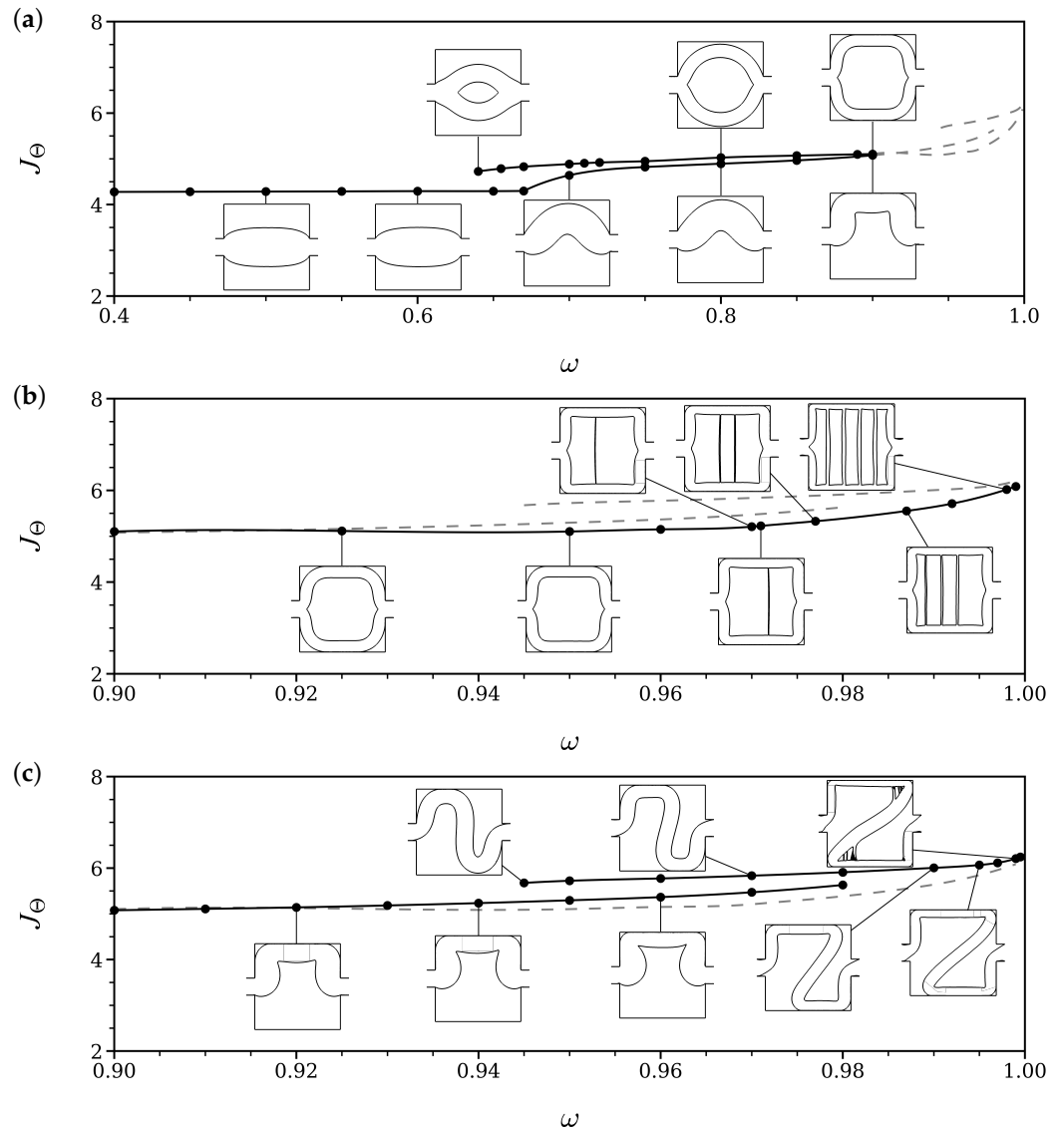


Figure 7. Optimal designs sorted by weighting ω for the two-dimensional single pipe device with heated walls presented in Figure 6. (a) Low and intermediated thermal weights. The dashed lines denote the results obtained at large thermal weights, further presented by the close-ups in (b,c) for (b) symmetric and (c) asymmetric designs.

For low thermal weights, the optimal design is a single, straight pipe connecting the inlet to the outlet as evidenced in Figure 8a. This is because the contribution of the thermal cost function is negligible, meaning that the sole objective of the algorithm is to minimize fluid power dissipation, which in turn yields wide, short pipes. In return, the optimal pipe is as wide as allowed by the volume constraint, though with an increased cross section halfway (compared to the inlet and outlet) to minimize shear. Increasing ω adds more priority to increase the recoverable thermal power, which opens the possibility to depart from the straight pipe even at the cost of some increase in the hydraulic objective. In this regard, our results highlight the existence of two distinct branches of solution, referred to as symmetric and asymmetric.

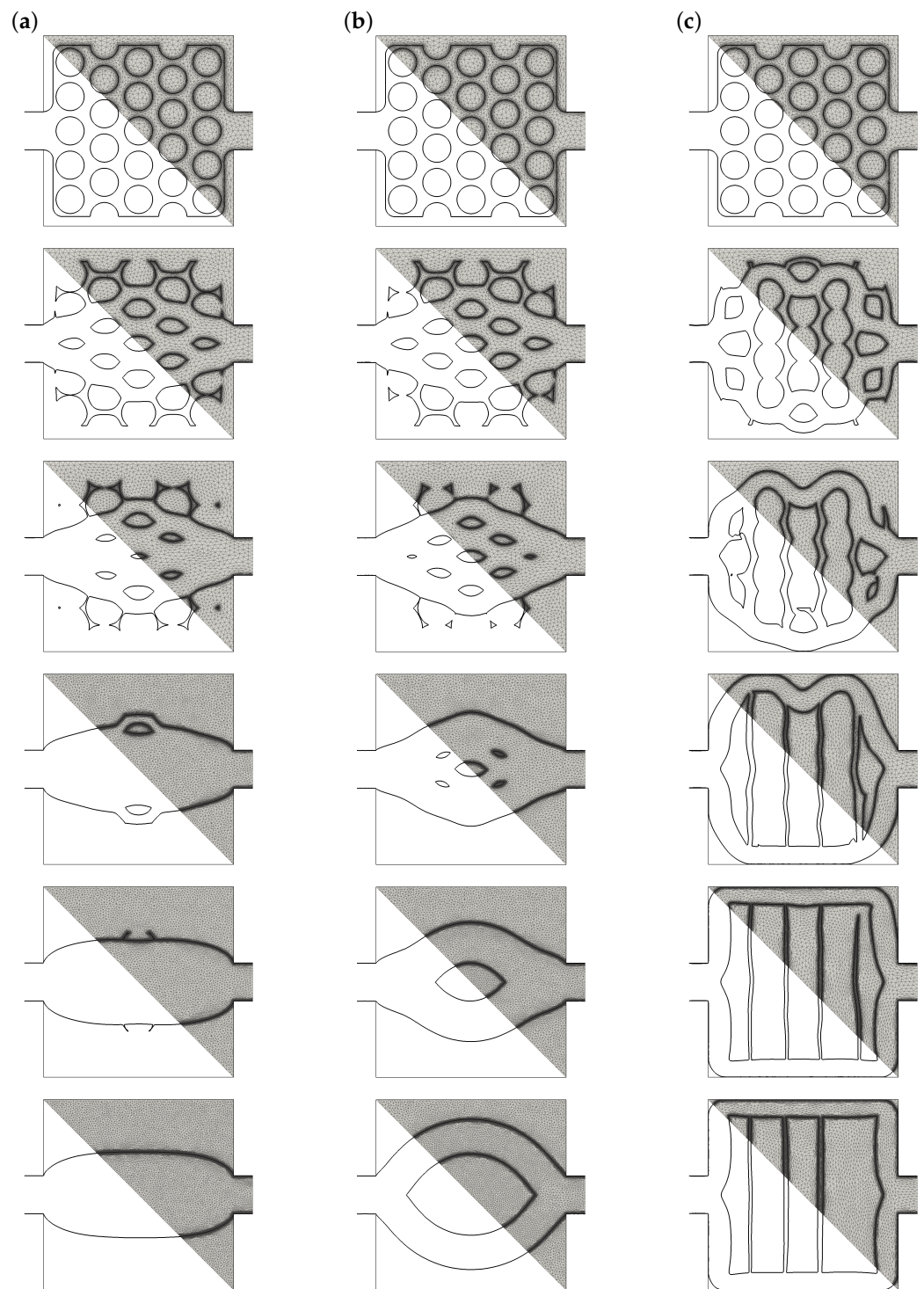


Figure 8. Multi-objective optimization of the two-dimensional single pipe device with heated walls presented in Figure 6. From top to bottom: the zero iso-value of the level set function and the corresponding anisotropic adapted meshes are sampled throughout the optimization process using the parameters outlined in Table 3. (a) Straight pipe solution with $\omega = 0.4$. (b) Solid core solution with $\omega = 0.7$. (c) Fragmented core solution with $\omega = 0.987$.

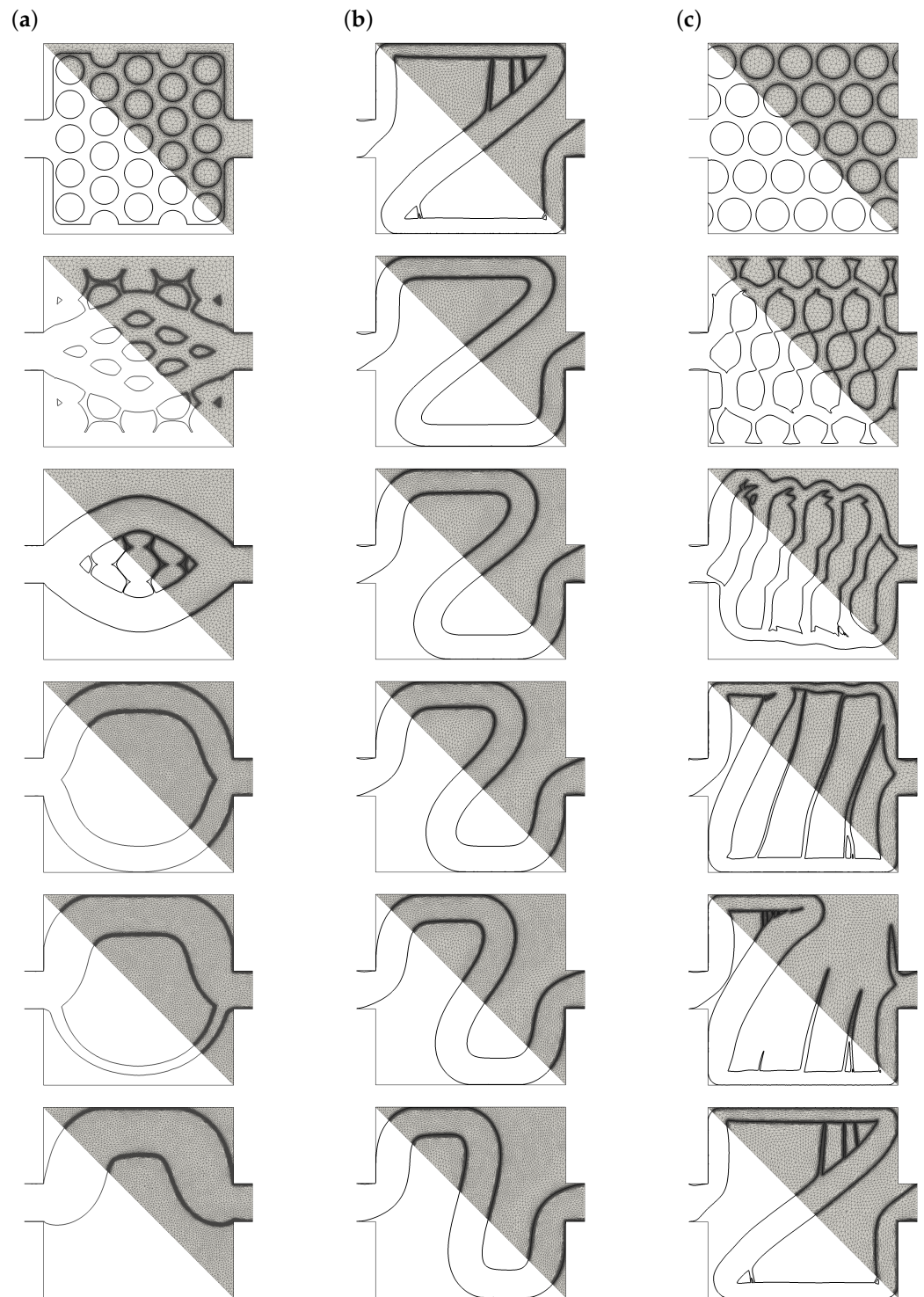


Figure 9. Multi-objective optimization of the two-dimensional single pipe device with heated walls presented in Figure 6. From top to bottom: the zero iso-value of the level set function and the corresponding anisotropic adapted meshes are sampled throughout the optimization process using the parameters outlined in Table 3. (a) Bent pipe solution with $\omega = 0.85$. (b) Z pipe solution with $\omega = 0.97$. (c) Fragmented Z pipe solution with $\omega = 0.998$.

All symmetric designs exhibit a solid core forming at the cavity center, thereby splitting the lead into upper and lower channels as shown in Figure 8b. This increases the dissipated power, as the distance covered by the fluid travels is lengthened, and increases even further the recoverable thermal power, as both pipes move towards the hot walls, which, given

the high thermal conductivity of the solid (10 times that of the fluid), allows to heat the fluid while minimizing the effects of conduction through the solid phase. The asymmetric designs presented in Figure 9a conversely feature a single pipe bending into either the lower or the upper half of the domain, which is a different trade-off involving both less recoverable thermal power and less dissipated power, as the fluid is heated up at only one out of the two hot walls but travels in a wider pipe.

Increasing the thermal weight forces the fluid along the hot walls to expand the exchange surface. Beyond a certain threshold, the symmetric solid core splits vertically into an increasing number of subcores, as a network of fluid strips forms to act as a large thermal resistance breaking the horizontal temperature gradient to reduce the core heat conduction; see Figure 8c. Meanwhile, in Figure 9b, the asymmetric bent pipe gives way to the more complex Z-shaped pipe successively forcing the flow along the top and bottom walls (yet another trade-off that increases both the recoverable thermal power and the dissipated power, as the heat exchange surface doubles, but the fluid travels in a thinner and longer pipe), whose solid layout eventually fragments vertically near the Z edges to make the most of the low conductivity of the fluid; see Figure 9c.

Upon comparing the above design to those in ref. [53] (the closest study to our work in the available literature), the following remarks can be made:

- Anisotropic adapted meshes dramatically improve the accuracy of all geometric representations, as most results in the recent available literature exhibit obvious staircase effects in all curved regions.
- The solid and fragmented core solutions are generally consistent, although they show up in [53] at surprisingly much lower values of ω (an issue already raised in [26]) and with lesser horizontal symmetry at large thermal weights (which may be because the authors in the aforementioned study do not impose a specific target volume of fluid but only an upper bound).
- Asymmetric designs are noticeably absent from [26,53] and from other studies tackling variations of this problem. Again, the explanation may lie in the constraint on the maximum volume of fluid, in the sense that for a given asymmetric design minimizing the cost function under a certain thermal weight, a more efficient symmetric design may exist at a smaller volume of fluid. Asymmetric designs are reported in [32], for which the authors allude to the use of unstructured meshes, but we believe they are rather the consequence of different flow regimes, as the aforementioned study considers a much higher Reynolds number of 400 and a much lower Prandtl number of 0.05, and the present use of unstructured meshes does not alter the solutions' symmetry.
- A similar formation of fluid strips to act like a heat insulation material at large ω is documented in [53]. While it is a robust mechanism, in the sense that even a non-fragmented solid cores and Z pipes computed at a slightly smaller thermal weight end up breaking up, we have found the solid layout splits to be very sensitive to the optimization path. This is evidenced in Figure 10 showing a series of fragmented core designs generated by varying the initial design under constant thermal weight. The number of subcores and the subcore arrangements do vary, but they yield identical cost functions (and thermal cost functions) within 1%, which suggests that fragmented solutions are actually flat minimizers.
- Non-physical designs (e.g., broken flow paths, dead ends and total fluid flow blockage, all highly undesirable from manufacturing point of view) have been obtained at much higher values of $\omega > 0.999$, which is when the contribution of the hydraulic cost function becomes negligible. This may have to do with the modeling of the solid material, as a porous medium does allow solutions with no fluid connection between the inlet and outlet flows, while the IVM rigorously forces the solid velocity to zero.

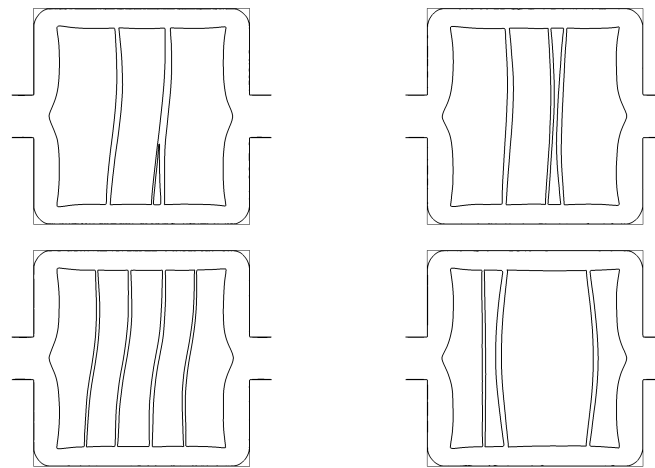


Figure 10. Fragmented core solutions computed under various initial designs under thermal weight $\omega = 0.987$.

Additional testing has been performed in the attempt to clarify the connection between the various branches of solutions (although not the intended scope of this study). The main findings are threefold: first, the straight pipe solution exists up to $\omega \sim 0.7$, after which its centerline shifts increasingly in the upper domain (or lower domain, by vertical reflectional symmetry) and the solution evolves continuously into the bent pipe solution. Second, the solid core solution branches off the straight pipe at about $\omega \sim 0.64$ (this has been estimated using a branch-tracking technique in which the design is initialized with a solid core solution computed at a slightly larger thermal weight), then evolves continuously into the fragmented core solution. Finally, the connection between the bent and Z pipe solutions remains uncertain: both solutions have been found to coexist over a range of thermal weights from 0.94 to 0.98, where they yield almost identical cost functions. Meanwhile, we could not manage to have a bent pipe continuously turn into a Z, regardless of the value of ω and the number of update steps (up to several ten thousands). This raises the possibility that the Z pipe solution may branch off subcritically from the bent pipe solution, leading to hysteresis (testing this hypothesis is not easy due to the difficulty of consistently generating Z pipe solutions unless a branch-tracking technique is used, which is why the optimization run documented in Figure 9b does not start from the classical design with solid occlusions).

Finally, Figure 11 presents the multi-objective Pareto front of all computed optimal solutions. Interestingly, it turns out that the Pareto-efficient subset consists exclusively of straight, bent and Z pipes (although the fragmented core solutions equally dominate at very high influences of the thermal objective function). Interestingly, the close-to-convex shape of the Pareto front means that a few solutions provide an acceptable trade-off by having both single cost functions close to their single objective optimization. This corresponds here to the bent pipe at $\omega = 0.97$ and the Z pipe at $\omega = 0.95$, for which the recoverable thermal power is below its single objective maximum by less than 10% (the dissipated power is 7 times as large as its single objective minimum, which is not small, strictly speaking, but very reasonable given that the worst performance is actually by a factor of 100).

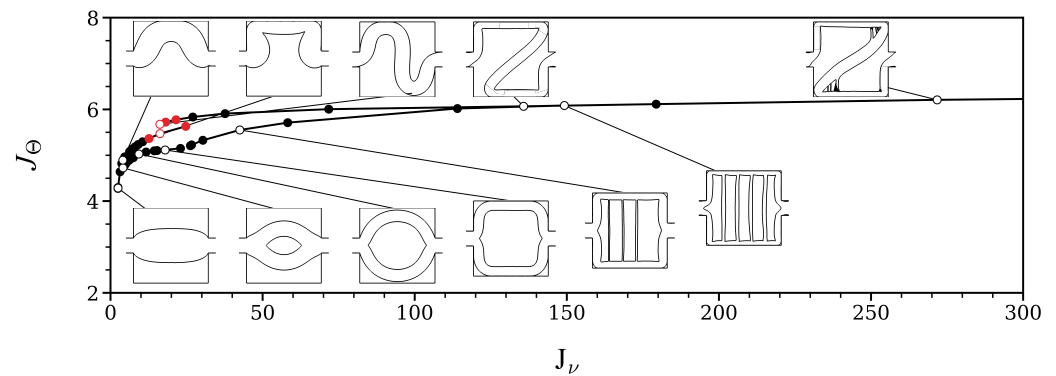


Figure 11. Bi-objective Pareto topology optimization of the single-pipe device with heated walls. The red symbols are the near-optimal design for which both the dissipated power and the recoverable thermal power approach their single objective optimization value.

6.4. Three-Dimensional Single Pipe with Heated Walls

The last test case stands as a three-dimensional counterpart to the two-dimensional conjugate heat transfer problem considered in Section 6.3. The setting inspired from [17] is depicted in Figure 12, with detailed problem parameters given in Table 4. The design domain is a rectangular cavity with a height of one and an aspect ratio of 2:1:1, with a single inlet (respectively, a single outlet) on the left (respectively, on the right), again lined up in front of each other. A cold fluid is flowing from the inlet and is heated by the cavity walls, with the difference being that only a finite stripe at the middle of the cavity walls is maintained at a constant (hot) temperature and all remaining walls (cavity and leads) are considered adiabatic. In what follows, the thermal weight is set to $\omega = 0.95$ to add more priority to increase the recoverable thermal power. Despite the configuration possessing two reflective symmetries, we opted not to reduce the computational effort by modeling only a quarter of the domain along with symmetry boundary conditions. This is feasible [58] but would preclude evaluating the method within the context of large-scale systems, so the full domain is discretized with 5,000,000 mesh elements, and we let symmetries potentially materialize as a result of the optimization.

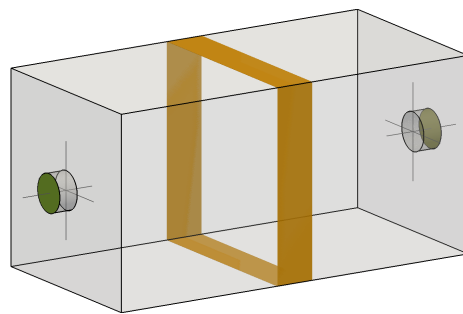


Figure 12. Set-up of the three-dimensional single-pipe problem with heated walls: one single hot stripe. The orange and light gray shades denote hot isothermal and adiabatic walls, respectively.

Table 4. Numerical parameters for the three-dimensional single-pipe problem with heated walls.

$\Omega = [0; 2] \times [0; 1] \times [0; 1]$	»	» Design domain
$d = 3$	»	» Problem dimensionality
$V_{target} = 0.4$	»	» Target volume of fluid
$V_{\varphi,0} = 1.8$	»	» Initial volume of fluid
$Re = 12$	»	» Reynolds number
$Pr = 83.5$	»	» Prandtl number
$k_s/k_f = 10$	»	» Thermal conductivity ratio
$T_w = 10$	»	» Hot stripe temperature
$\Delta x_h = 0.2$	»	» Hot stripe width
$x_{h1} = 1$	0.5	» Hot stripe 1 center coordinate
-	-	$x_{h2} = 1.5$ Hot stripe 2 center coordinate
$u_i = 1$	»	» Inlet centerline velocity
$T_i = 0$	»	» Inlet cold temperature
$e = 0.2$	»	» Inlet diameter
$l_i = 0.1$	»	» Inlet leads length
$\mathbf{x}_i = (-0.1, 0.5, 0.5)$	»	» Inlet center coordinates
$u_o = 1$	»	» Outlet centerline velocity
$e_o = 0.2$	»	» Outlet diameter
$l_o = 0.1$	»	» Outlet lead length
$\mathbf{x}_o = (2.1, 0.5, 0.5)$	»	» Outlet 1 center coordinates
$N_n = 1,000,000$	»	» Nb. mesh nodes
$N_{el} = 5,000,000$	»	» Nb. mesh elements

The initialization shown in Figure 13 corresponds to a fluid box filled with islands of solid spherical inclusions occupying about 10% of the cavity. The fluid thus initially fills 90% of the cavity, well above the 40% volume constraint; hence, the same approach as in Section 6.2 is used, in which the constraint value decreases during the early stage of the optimization process until it reaches the target within the required precision. Once more, the method demonstrates proficient handling of the diverse topological modifications encountered throughout the optimization process. All anisotropic adapted meshes feature highly elongated elements, irrespective of the interface complexity. These elements enable the precise delineation of the fluid and solid domains, including the edges of the hot stripe, and facilitate accurate computation of solutions at all optimization stages. In the optimal solution shown in Figure 13, the fluid flows in and out of the cavity through single, straight pipes. This is because the hot stripe is far from the inlet/outlet sections, so there is a good proportion of the cavity where the thermal cost function contributes little to nothing, and the best trade-off is to minimize power dissipation. Similarly to what could be observed in 2-D, a solid core forms in the stripe region. The latter divides the inlet pipe into a near-perfect symmetrical network of eight pipes that quickly merge themselves to deliver the fluid to the outlet via a complex four-element comb-like arrangement (one per face of the cavity). This forces the fluid along the hot walls, eventually merging into a thin square annulus shaped to the hot stripe to maximize the fluid heat-up. As illustrated in Figure 14, the optimal layout includes slender fluid inclusions attached to the main pipes. This is essentially reminiscent of the two-dimensional fragmentation mechanism observed at such a large thermal weight, where fluid is employed to thermally insulate the inner pipes from the (cold) inlet temperature. The present optimal design is overall close to that documented in [17], but the pipe arrangements differ in the hot region, most likely because the authors in the aforementioned reference optimized the thermal recoverable power by imposing an upper bound threshold for the pressure drop (which yields a different trade-off).

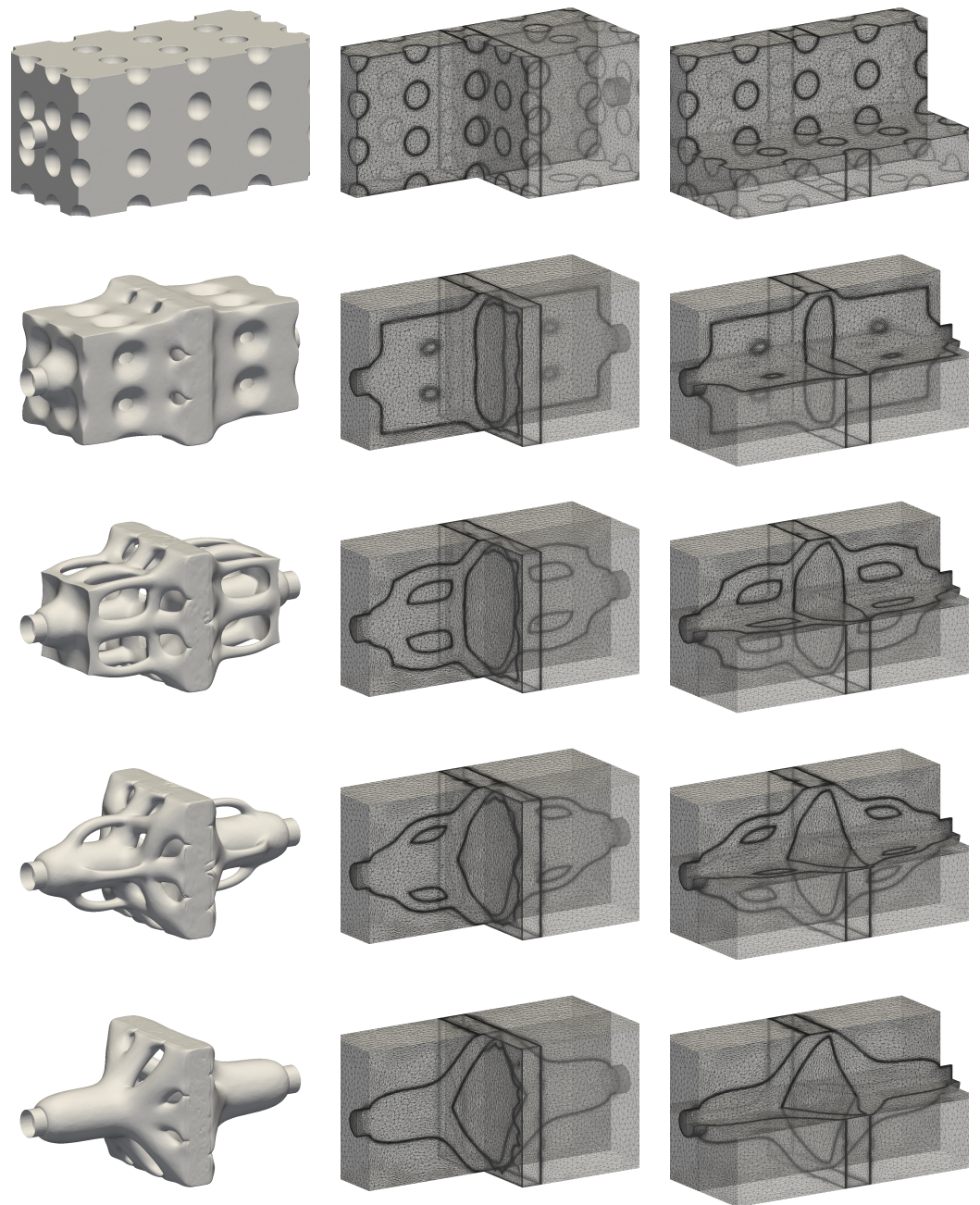


Figure 13. Multi-objective optimization of the three-dimensional single pipe device with heated walls (one single hot stripe) presented in Figure 12. The zero iso-value of the level set function and the corresponding anisotropic adapted meshes are sampled throughout the optimization process using the parameters outlined in Table 4. The volume of the fluid domain in each layout is 90%, 42.9%, 20.6%, 20.5% and 20.4%, respectively.

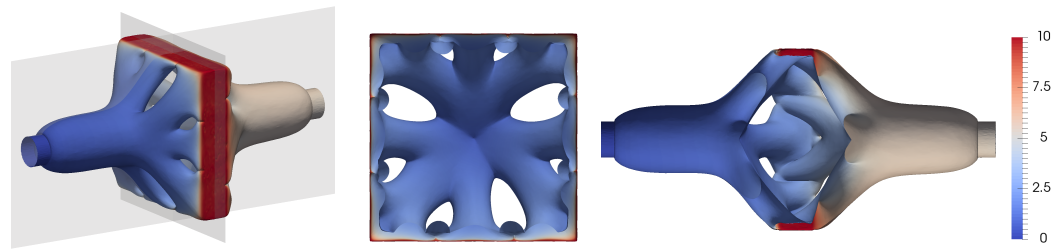


Figure 14. Optimal design of the three-dimensional single pipe device with heated walls (one single hot stripe) presented in Figure 12, together with stream-wise and cross-wise cuts at positions shown by the grey planes. The hue of the colors corresponds to the temperature profile.

Two other cases have been considered to assess the capability of designing more complex shapes by giving more importance to the thermal cost function. The associated set-ups depicted in Figure 15 differ by the number and position of hot stripes, namely, the first case (case 1) has one stripe shifted upstream against the inlet, and the second one (case 2) has two stripes against the inlet and outlet arranged symmetrically with respect to the middle of the cavity; see Table 4 for the provision of other detailed problem parameters, and Figures 16 and 17 for an illustration of the corresponding optimization runs using anisotropic adapted meshes. For case 1, the main features of the baseline optimal discussed hereinabove carry over, with the difference that the solid core moves upstream to follow in the footsteps of the hot stripe; hence, the inlet lead immediately splits into a similar network of eight pipes. For case 2, the presence of two separated hot spots yields a different optimal, with the eight pipes reconfiguring into four wider pipes to transport fluid the shortest way downstream and avoid the cost of bending. These pipes then widen to form four quasi triangular prisms shaped to the downstream stripe (to maximize the fluid heat up) before merging to connect to the outlet. In both cases, the optimal layouts shown in Figure 18 showcase similar slender fluid inclusions attached to the main pipes to capitalize on the insulating properties of the low conductivity fluid.

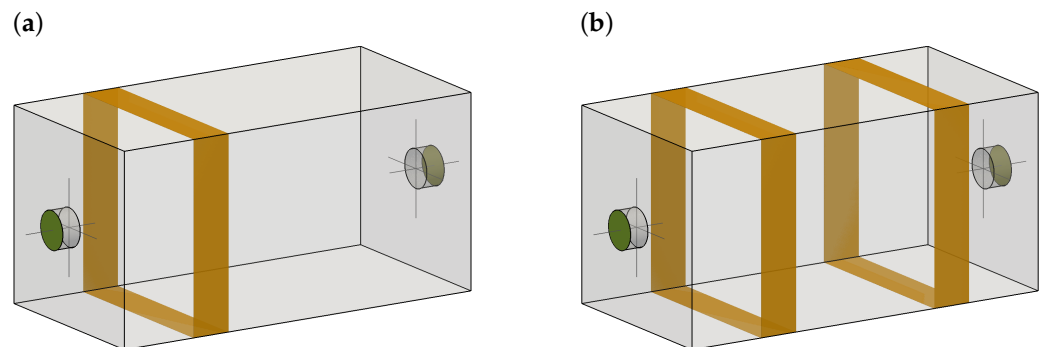


Figure 15. Set-up of the three-dimensional single-pipe problem with heated walls: one single upstream hot stripe (a) vs. two hot stripes (b). The orange and light gray shades denote hot isothermal and adiabatic walls, respectively.

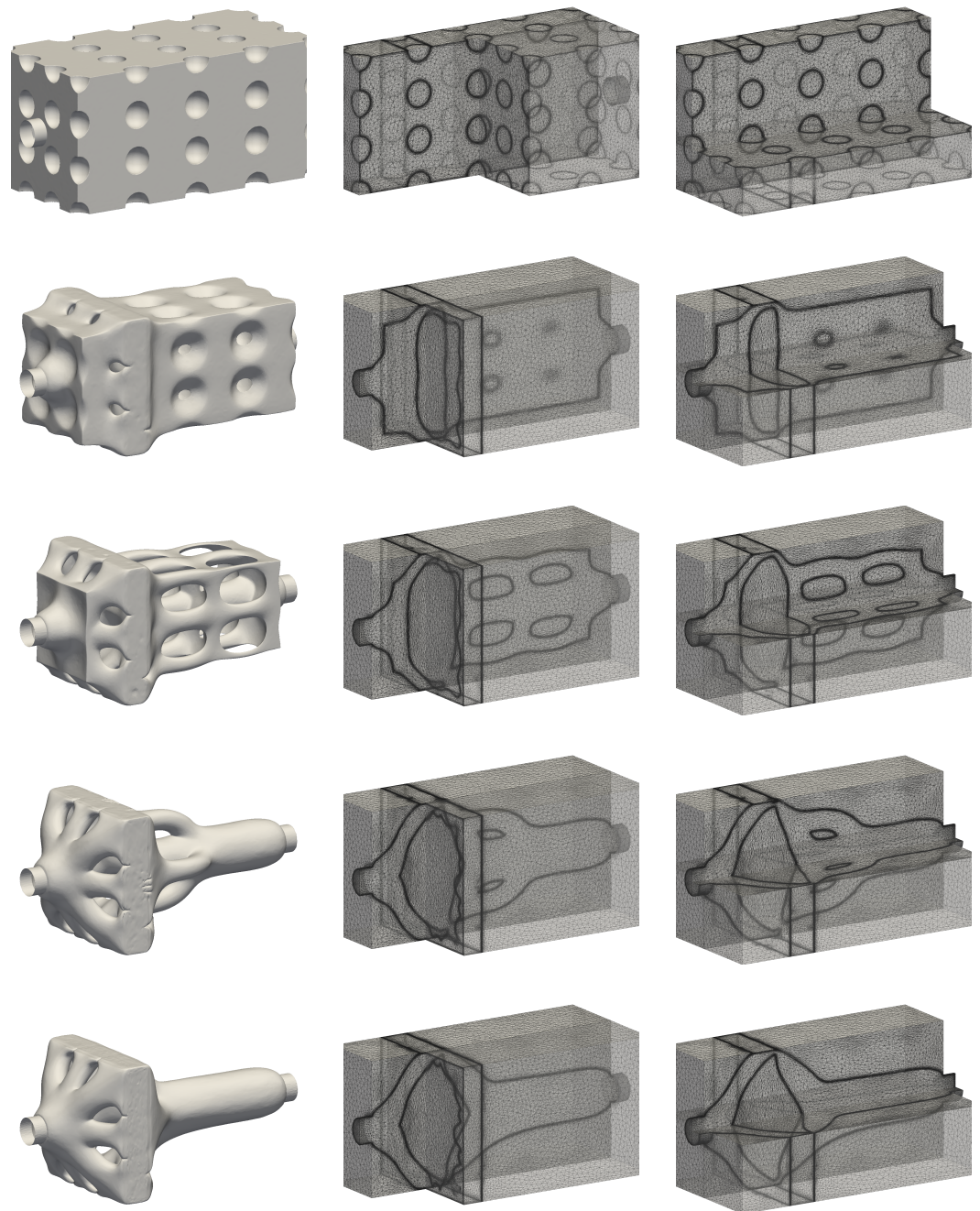


Figure 16. Multi-objective optimization of the three-dimensional single pipe device with heated walls (one single upstream hot stripe) presented in Figure 15a. The zero iso-value of the level set function and the corresponding anisotropic adapted meshes are sampled throughout the optimization process using the parameters outlined in Table 4. The volume of the fluid domain in each layout is 90%, 43.0%, 20.4%, 20.5% and 20.4%, respectively.

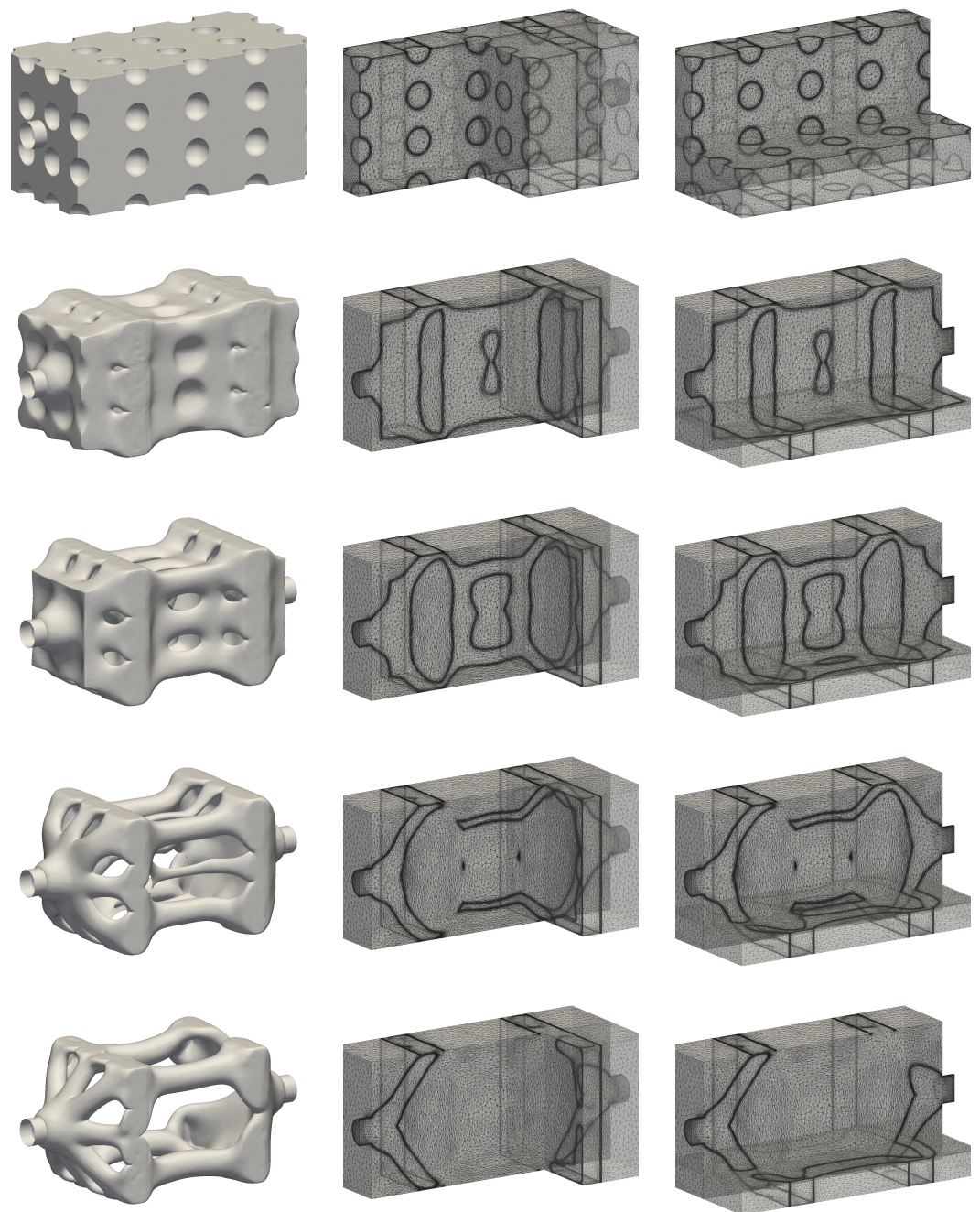


Figure 17. Multi-objective optimization of the three-dimensional single pipe device with heated walls (two hot stripes) presented in Figure 15b. The zero iso-value of the level set function and the corresponding anisotropic adapted meshes are sampled throughout the optimization process using the parameters outlined in Table 4. The volume of the fluid domain in each layout is 90%, 54.4%, 31.9%, 20.6% and 20.3%, respectively.

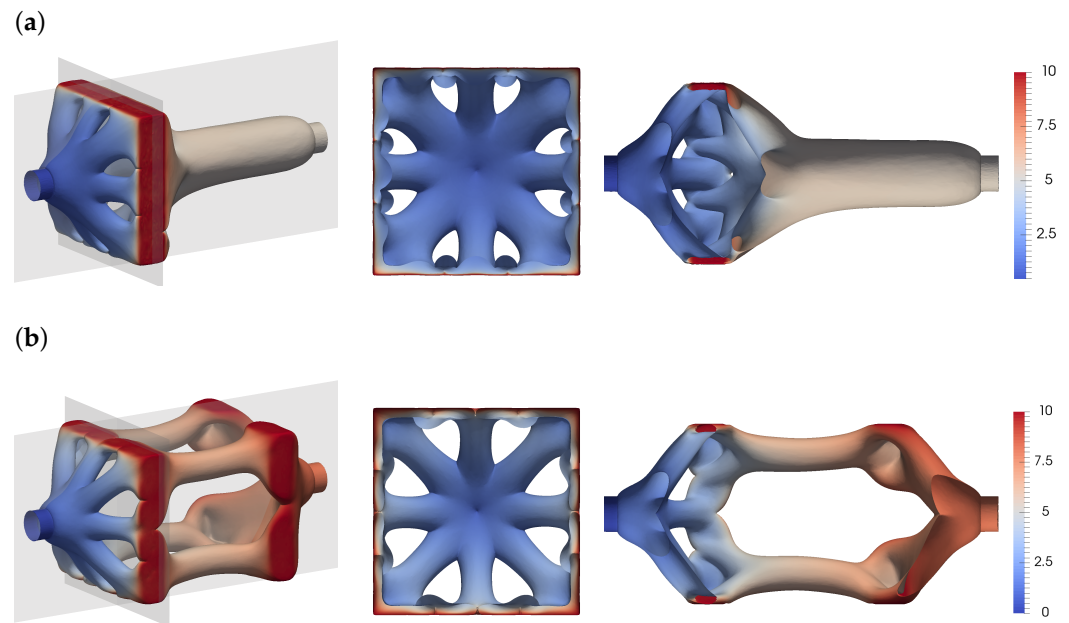


Figure 18. (a) Optimal design of the three-dimensional single pipe device with heated walls (one single upstream hot stripe) presented in Figure 15a, together with stream-wise and cross-wise cuts at positions shown by the grey planes. (b) Same as (a) for the device with heated walls (two hot stripes) presented in Figure 15b. The hue of the colors corresponds to the temperature profile.

7. Discussion

7.1. Numerical Cost

In detail, the number of mesh nodes utilized here turns out to be oversized, which is primarily beneficial during the initial optimization phase, where large interface surface areas (or perimeters in 2-D) must be accurately represented due to the presence of numerous solid inclusions. This surface area, however, decreases considerably after the first few dozen iterations, as was determined by computing numerically the surface area as

$$S_\varphi = \int_{\Omega} \delta_\epsilon(\varphi) \, dv, \tag{32}$$

where δ_ϵ is the Dirac function

$$\delta_\epsilon(\varphi) = \begin{cases} \frac{1}{2\epsilon} \left(1 + \cos\left(\pi \frac{\varphi}{\epsilon}\right) \right) & \text{if } |\varphi| \leq \epsilon, \\ 0 & \text{if } |\varphi| > \epsilon, \end{cases} \tag{33}$$

that has undergone smoothing with the same regularization parameter ϵ as the Heaviside function defined in Equation (13). Additionally, the mesh is refined based on the hierarchical importance of the level set gradient, meaning that it automatically coarsens in low-gradient regions whenever new geometrical features materialize in the solution, as those are associated with high gradients and thus require additional refinement. If the number of nodes is large, having lower interface surface areas enables the resolution of finer, more complex patterns without compromising accuracy in other parts of the design domain, as the coarsened regions are already over-resolved. This progression is evident through the gradual mesh refinement in the fluid domain depicted in various figures, as more elements become available to enhance the mesh in other regions of the domain.

For each multi-objective conjugate heat transfer case considered herein, we detail in Figure 19 the timing results averaged from 100 dedicated update steps (in 3-D settings, 200 steps in 2-D) performed on 64 cores (AMD EPYC 7502 2.5 GHz bi-processors, 256 Go RAM, AMD, Santa Clara, CA, USA). All results were normalized a posteriori to yield a unit average time per iteration. In 2-D, the cost of an iteration is primarily that of computing the

state solution (this represents about 55% of the overall cost, corresponding to approximately 10 Navier–Stokes iterations), and secondarily that of adapting the mesh (20% of the overall cost). When running on the same number of processors, the cost associated with a 3-D iteration exceeds its 2-D counterpart by approximately three orders of magnitude. This is predominantly due to the high computational effort associated with the two passes of mesh adaptation. Those account for about 70% of the overall cost, although the first pass is more time consuming, which is to be expected given that (i) the volume constraint is not enforced at each design step, only when the discrepancy between the actual and target volumes exceeds the 5% threshold, and (ii) fewer mesh elements and nodes need to be moved during the second pass. Interestingly, the cost of reinitializing the level set function and of optimizing the volume constraint offset remains very manageable, as the 4–5 iterations required to achieve the intended accuracy ultimately account for less than 2% of the overall cost. Note, all 3-D cases yield almost identical timing results. The sole distinction lies in the effort associated with the volume constraint step, as the geometric characteristics of the layout being studied directly impact the frequency of consecutive corrections applied. This suggests that similar conclusions may extend to other channel flow problems addressed with similar parameters. The close similarity carries over to the absolute run times per iteration shown in Figure 20. This implies that the total run times in Table 5 are primarily influenced by the number of steps required for convergence, which, in turn, depends on the number of steps needed to restore the proper volume of fluid. The reported run times are significant on their own, but we did not try to optimize efficiency, which can be performed by adjusting the initial layouts (multiple inclusions were utilized intentionally to demonstrate the method capability to support complex topological changes) or by fine-tuning the descent factor (the only requirement here is that the displacement at each step should not exceed the level set cut-off thickness so as to accurately track the evolved interface). Moreover, those run times are considerably lower than those required to converge on a fixed uniform grid with comparable refinement. For context, discretizing the single inlet/single outlet case on a uniform grid with an element size of 5×10^{-3} would necessitate approximately 140 million elements, yet this would not be adequate to match the interface value achieved using the present anisotropic meshes.

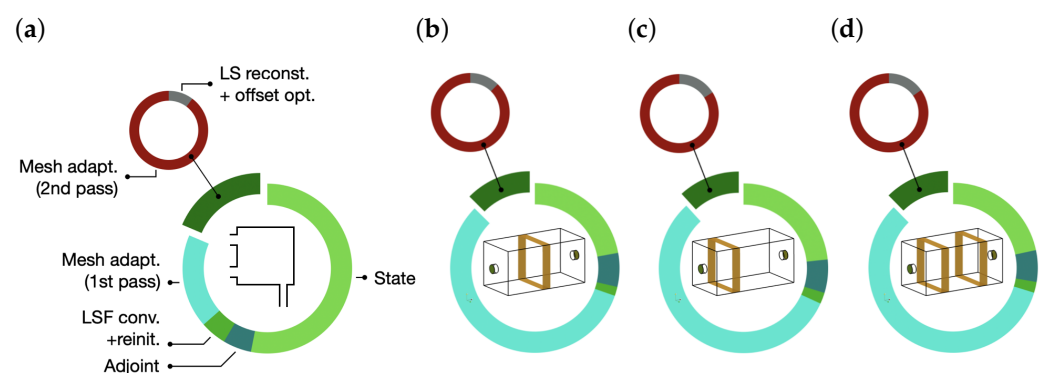


Figure 19. (a) Computational cost of the topology optimization algorithm, measured by as the average of 200 update steps of the 2-D single-pipe problem with heated walls shown in Figure 2. (b) Same as (a) for 100 update steps of the 3-D single-pipe problem with one centered hot stripe shown in Figure 12. (c,d) Same as (b) for the 3-D single-pipe problem with (c) one upstream hot stripe and (d) two hot stripes shown in Figure 15. The LSF (respectively, LS) label stands for filtered level set (respectively, level set).

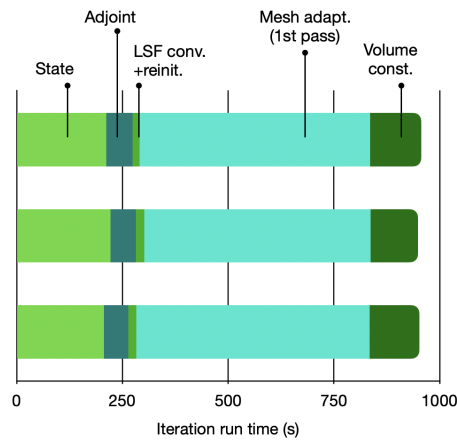


Figure 20. Average computing time per iteration for the 3-D single-pipe problems detailed in Figure 19.

Table 5. Run times for the various 3-D cases documented in Figure 19.

64	»	»	Nb. cores
270 h	340 h	240 h	Run time
800	1000	700	Nb. design steps
200	200	200	Nb. steps to target volume

7.2. High-Reynolds-Number Flows

We keep in mind that all cases reported herein are low-Reynolds number cases, making the approach very relevant for a broad range of microfluidic applications, for instance, the optimal design of microchannel heat sinks. Conversely, the significance of the computed optima as solutions to actual industrial heat exchanger problems is questionable, given the high Reynolds numbers at play. It lies out of the scope to tackle such cases right away, as the adjoint-based sensitivity analysis of high-Reynolds-number flow has its challenges, including the need to evaluate all sensitivities from time-dependent adjoint solutions to be solved repeatedly backwards in time, which becomes nearly intractable in three dimensions without implementing advanced checkpointing, interpolation, and/or integration techniques. Relevance is thus assessed a posteriori by performing high-Reynolds-number simulations of several shapes generated over the course of optimization (the only requirement being that the volume of fluid constraint be satisfied). Results are reported here for the one single upstream hot stripe case presented in Figure 15, for which 800 time steps were carried out at $Re = 1.2 \times 10^4$, after which the cost function was averaged over an additional 200 time steps. The simulations use the exact same CFD environment, without additional turbulence modeling since the fine scale of the VMS solution acts de facto as an implicit large eddy simulation). The results pertaining to the last three shapes in Figure 16 are reported in Table 6, together with their baseline counterparts obtained at $Re = 12$. We also provide in Figure 21 3-D instantaneous streamlines colored by the temperature to emphasize that the flow undergoes an increasingly complex swirling motion after crossing the solid core, which keeps being accurately resolved by virtue of the anisotropic mesh adaptation procedure. While the cost function increases with Re (which was found to be because the optimal heat transfer performance decreased), it is interesting to note that the optimal shape keeps performing best even at such a high Reynolds number, and that its superiority with respect to the other two shapes is more pronounced (the improvement in the cost function being, respectively, by 8.5% and 1.8% at $Re = 12$, but 15.2% and 2.5%

at $Re = 1.2 \times 10^4$). This suggests that the present approach can deliver relevant robust and practical solutions to real-life heat exchanger applications.

Table 6. Performance of the optimal layouts under various high-Reynolds-number settings. All cost function evaluations are normalized using the inlet maximum velocity and diameter (or equivalently, using $\rho u_i^3 e_i^2$ as the reference cost functional value).

			
1.74	1.62	1.59	$Re = 12$
2.23	1.94	1.89	$Re = 1.2 \times 10^4$

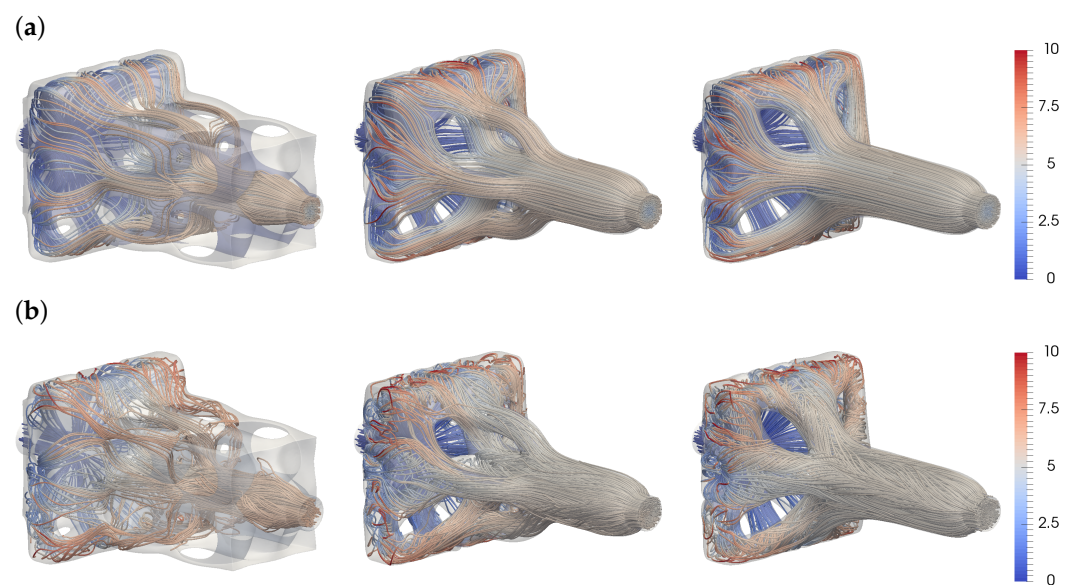


Figure 21. (a) Representative steady 3-D streamlines colored by the temperature computed at $Re = 12$ for the last three shapes in Figure 16 by the magnitude of velocity. (b) Same as (a) for the instantaneous streamlines computed at $Re = 1.2 \times 10^4$.

8. Conclusions

The current study demonstrates the feasibility of using anisotropic meshes adapted to perform the topology optimization of conjugate heat transfer systems while operating under the constraint of a fixed number of nodes. The proposed method integrates a level set method to delineate the interface between the fluid and solid sub-domains based on the zero iso-value of a signed distance function, along with stabilized weak forms of the state, adjoint, and level set transport equations formulated and solved in the variational multi-scale (VMS) framework. Such an approach has the capability to accommodate the significant topological changes occurring over the course of optimization. However, its primary advantage over existing methods lies in its ability to accurately capture all interfaces using adapted meshes whose anisotropy matches that of the numerical solutions. By doing so, it considerably reduces the cost associated with enhancing numerical precision, as increasing the number of nodes is only necessary in the direction of anisotropy. In return, only twice as many nodes are needed to double the resolution, as opposed to the four- and eightfold increases in classical 2-D and 3-D isotropic computations.

The method has undergone testing across various instances of bi-objective minimization, prioritizing high recoverable thermal power and low power dissipation. This includes a series of 3-D examples encompassing several tens of millions of state degrees of freedom.

The resulting optimal layouts align closely with the findings in the existing literature, which suggests that the method holds promise for efficiently engineering diverse low-mass, high-efficiency thermal devices such as heat exchangers, heat sinks, or cold plates while facilitating the transition to manufacturable CAD models almost identical to the numerical optima. Moreover, this holds true even at non-negligible Reynolds numbers as confirmed through dedicated simulations comparing the performance of different shapes generated throughout the optimization iterations.

The present approach can be used as multi-objective topology optimization strategy for a broad range of thermal devices, for which one seeks to achieve a thermal technical target while reducing the system energy consumption. Thermal control can aim at increasing heat transfer (as was performed here), but also enhance temperature uniformity, or reduce temperature and/or heat flux fluctuations. The objective in terms of flow resistance is often to diminish the power dissipation of the fluid, which can lead to different formulations, as low dissipation is generally correlated with low drag and pressure drops. All such objectives are tractable using the exact same numerical framework, provided the optimization problem is formulated with a moderate number of equality constraints, and that all cost functions can be expressed as integrals over all or any part of the inlet and/or outlet (not the wall, as is the case here, which yields homogeneous adjoint equations with non-homogeneous boundary conditions), or over any part of the computational domain (which leads to non-homogeneous adjoint equations with homogeneous boundary conditions). The method can also easily accommodate more complex objectives aiming at improving the thermal performance while minimizing dissipation and achieving even flow rates in distinct branches of a network (by minimizing the distance to a target velocity distribution), which is of great interest to design high-performance lab-on-a-chip microfluidic devices.

Future work should aim at improving the numerical efficiency, for instance, by adding nucleation mechanisms to alleviate the need for an initial design with holes, as this makes it difficult to fulfill the proper volume constraint from the outset, and requires substantial mesh refinement to avoid clogging the fluid path in the early stage of optimization. Other research directions include application to complex physics more representative of real-life situations (e.g., multiphase flows and fluid–structure interactions), as well as the assessment of multi-component mesh adaptation criteria to further improve the accuracy of the gradient evaluations by encompassing the discrepancy in the spatial supports of the state and adjoint fields.

Author Contributions: Conceptualization, E.H.; methodology, E.H. and P.M.; software and validation, E.H., P.M. and W.A.N.; formal analysis, E.H. and P.M.; investigation, W.A.N.; resources, E.H.; data curation, W.A.N.; writing—original draft preparation, P.M.; writing—review and editing, E.H., P.M., D.L., D.S. and W.A.N.; visualization, E.H., P.M. and W.A.N.; supervision, E.H., P.M. and D.S.; project administration, D.L., E.H. and D.S.; funding acquisition, D.L. and D.S. All authors have read and agreed to the published version of the manuscript.

Funding: This work is part of the PANTTHER project that has received funding from the Clean Sky2 Joint Undertaking (JU) under grant agreement No 886698. The JU receives support from the European Union’s Horizon 2020 research and innovation program and the Clean Sky 2 JU members other than the Union. It reflects only the authors’ view and the JU is not responsible for any use that may be made of the information it contains.

Data Availability Statement: The data presented in this study are available on reasonable request from the corresponding author. The data are not publicly available due to confidentiality reasons.

Conflicts of Interest: Author Damien Serret was employed by the company TEMISTh SAS, Technocentre des Florides. All authors declare that the research was conducted in the absence of any commercial or financial relationships that could be construed as a potential conflict of interest.

Appendix A. Adjoint-Based Sensitivity Analysis

Appendix A.1. General Setting

This initial appendix outlines the adjoint method utilized to compute the cost function sensitivity to a design variable β , taken to model local surface normal displacements of the solid–fluid interface. In what follows, the solid is characterized by the sole thermal conductivity k_s , and the fluid by its density ρ_f , dynamic viscosity μ_f , thermal conductivity k_f and thermal heat capacity c_{p_f} . The incompressible Navier–Stokes and heat equations are used as governing equations of the flow problem, whose steady solutions in Ω_f satisfy

$$\nabla \cdot \mathbf{u} = 0 \quad \text{in } \Omega_f, \tag{A1}$$

$$\rho_f \mathbf{u} \cdot \nabla \mathbf{u} = -\nabla p + \nabla \cdot (2\mu_f \boldsymbol{\varepsilon}(\mathbf{u})) \quad \text{in } \Omega_f, \tag{A2}$$

$$\rho_f c_{p_f} \mathbf{u} \cdot \nabla T_f = \nabla \cdot (k_f \nabla T_f) \quad \text{in } \Omega_f. \tag{A3}$$

Open flow boundary conditions

$$\mathbf{u} = \mathbf{u}_i \quad \text{on } \Gamma_i, \tag{A4}$$

$$T_f = T_i \quad \text{on } \Gamma_i, \tag{A5}$$

$$\mathbf{u} = \mathbf{u}_o \quad \text{on } \Gamma_o, \tag{A6}$$

$$\nabla T_f \cdot \mathbf{n} = 0 \quad \text{on } \Gamma_o, \tag{A7}$$

are used, corresponding to prescribed inlet temperature and parabolic velocity distribution, zero heat flux at the outlet and prescribed outlet parabolic velocity distribution, and zero interface velocity, together with a (Robin) convective heat flux condition. This yields

$$\mathbf{u} = \mathbf{0} \quad \text{on } \Gamma, \tag{A8}$$

$$k_f \nabla T_f \cdot \mathbf{n} = \eta(T_f - T^*) \quad \text{on } \Gamma, \tag{A9}$$

where T^* denotes a reference temperature, and the amount of heat exchanged by the solid and fluid subdomains is governed by the heat transfer coefficient η . Indeed, it is commonly acknowledged that neither isothermal nor isoflux boundary conditions can adequately replicate real-world, practical heat transfer models, which is all the more true when the solid and fluid thermal diffusivities are comparable in magnitude [59].

The continuous adjoint method [36–38] is utilized to address the challenge of minimizing the cost function while holding to the coupled Navier–Stokes and heat equations as state equations. As a first step, the Lagrangian function is formed, here

$$\begin{aligned} \mathcal{L} = & \int_{\Gamma_i \cup \Gamma_o} J \, ds - \int_{\Omega_f} \tilde{p} \nabla \cdot \mathbf{u} \, dv - \int_{\Omega_f} \tilde{\mathbf{u}} \cdot (\rho_f \mathbf{u} \cdot \nabla \mathbf{u} + \nabla p - \nabla \cdot (2\mu_f \boldsymbol{\varepsilon}(\mathbf{u}))) \, dv \\ & - \int_{\Omega_f} \tilde{T}_f \cdot (\rho_f c_{p_f} \mathbf{u} \cdot \nabla T_f - \nabla \cdot (k_f \nabla T_f)) \, dv. \end{aligned} \tag{A10}$$

In this set-up, the adjoint pressure \tilde{p} serves as the Lagrange multiplier for the continuity Equation (A1), and the adjoint velocity $\tilde{\mathbf{u}}$ and temperature \tilde{T}_f act similarly to the Lagrange multipliers for the momentum and heat Equations (A2) and (A3). The objective is then to decompose the variation of \mathcal{L} resulting from a change in the interface position into individual variations with respect to the adjoint, state, and design variables. The one variation with respect to the adjoint solutions is given by

$$\begin{aligned} \delta_{(\tilde{\mathbf{u}}, \tilde{p}, \tilde{T}_f)} \mathcal{L} = & - \int_{\Omega_f} \delta \tilde{p} \nabla \cdot \mathbf{u} \, dv - \int_{\Omega_f} \delta \tilde{\mathbf{u}} \cdot (\rho_f \mathbf{u} \cdot \nabla \mathbf{u} + \nabla p - \nabla \cdot (2\mu_f \boldsymbol{\varepsilon}(\mathbf{u}))) \, dv \\ & - \int_{\Omega_f} \delta \tilde{T}_f \cdot (\rho_f c_{p_f} \mathbf{u} \cdot \nabla T_f - \nabla \cdot (k_f \nabla T_f)) \, dv, \end{aligned} \tag{A11}$$

and is thus zero since the triplet (\mathbf{u}, p, T_f) is a solution to the state equations, in which case the Lagrangian reduces to the cost function. After performing integration by parts, the one variation with respect to the state solutions is expressed as

$$\begin{aligned} \delta_{(\mathbf{u}, p, T_f)} \mathcal{L} = & \int_{\Omega_f} (\nabla \cdot \tilde{\mathbf{u}}) \delta p \, dv \\ & + \int_{\Omega_f} (-\rho_f \mathbf{u} \cdot \nabla \tilde{\mathbf{u}} + \rho_f \nabla \mathbf{u}^T \cdot \tilde{\mathbf{u}} - \nabla \tilde{p} - \nabla \cdot (2\mu_f \boldsymbol{\varepsilon}(\tilde{\mathbf{u}})) - \rho_f c_{p_f} T_f \nabla \tilde{T}_f) \cdot \delta \mathbf{u} \, dv \\ & + \int_{\Omega_f} (\rho_f c_{p_f} \mathbf{u} \cdot \nabla \tilde{T}_f + \nabla \cdot (k_f \nabla \tilde{T}_f)) \delta T_f \, dv \\ & + \int_{\Gamma_i \cup \Gamma_o} \partial_{\mathbf{u}} J \cdot \delta \mathbf{u} \, ds + \int_{\partial \Omega_f} (\tilde{p} \mathbf{n} + 2\mu_f \boldsymbol{\varepsilon}(\tilde{\mathbf{u}}) \cdot \mathbf{n} + \rho_f (\mathbf{u} \cdot \mathbf{n}) \tilde{\mathbf{u}} + \rho_f c_{p_f} T_f \tilde{T}_f \mathbf{n}) \cdot \delta \mathbf{u} \, ds \\ & - \int_{\Gamma_i \cup \Gamma_o} \partial_p J \mathbf{n} \cdot (-\delta p \mathbf{n} + 2\mu_f \boldsymbol{\varepsilon}(\delta \mathbf{u}) \cdot \mathbf{n}) \, ds - \int_{\partial \Omega_f} \tilde{\mathbf{u}} \cdot (-\delta p \mathbf{n} + 2\mu_f \boldsymbol{\varepsilon}(\delta \mathbf{u}) \cdot \mathbf{n}) \, ds \\ & + \int_{\Gamma_i \cup \Gamma_o} \partial_{T_f} J \delta T_f \, ds + \int_{\partial \Omega_f} ((k_f \nabla \tilde{T}_f \cdot \mathbf{n} + \rho_f c_{p_f} (\mathbf{u} \cdot \mathbf{n}) \tilde{T}_f) \delta T_f - k_f \tilde{T}_f \nabla \delta T_f \cdot \mathbf{n}) \, ds, \end{aligned} \quad (\text{A12})$$

where we have simplified due to the normal component in the viscous stress being zero in incompressible flows. In order to enforce $\delta_{(\mathbf{u}, p, T_f)} \mathcal{L} = 0$, all boundary and domain integrals must be zero in (A12). This allows formulating adjoint equations under the form of the linear, homogeneous problem

$$\nabla \cdot \tilde{\mathbf{u}} = 0 \quad \text{in } \Omega_f, \quad (\text{A13})$$

$$-\rho_f \mathbf{u} \cdot \nabla \tilde{\mathbf{u}} + \rho_f \nabla \mathbf{u}^T \cdot \tilde{\mathbf{u}} = \nabla \tilde{p} + \nabla \cdot (2\mu_f \boldsymbol{\varepsilon}(\tilde{\mathbf{u}})) + \rho_f c_{p_f} T_f \nabla \tilde{T}_f \quad \text{in } \Omega_f, \quad (\text{A14})$$

$$-c_{p_f} \mathbf{u} \cdot \nabla \tilde{T}_f = \nabla \cdot (k_f \nabla \tilde{T}_f) \quad \text{in } \Omega_f, \quad (\text{A15})$$

together with adjoint boundary conditions

$$\tilde{\mathbf{u}} = -\partial_p J \mathbf{n} \quad \text{on } \Gamma_i, \quad (\text{A16})$$

$$\tilde{T}_f = 0 \quad \text{on } \Gamma_i, \quad (\text{A17})$$

$$\tilde{\mathbf{u}} = -\partial_p J \mathbf{n} \quad \text{on } \Gamma_o, \quad (\text{A18})$$

$$k_f \nabla \tilde{T}_f \cdot \mathbf{n} + \rho_f c_{p_f} (\mathbf{u} \cdot \mathbf{n}) \tilde{T}_f = -\partial_{T_f} J \quad \text{on } \Gamma_o, \quad (\text{A19})$$

$$\tilde{\mathbf{u}} = \mathbf{0} \quad \text{on } \Gamma, \quad (\text{A20})$$

$$k_f \nabla \tilde{T}_f \cdot \mathbf{n} = \eta \tilde{T}_f \quad \text{on } \Gamma, \quad (\text{A21})$$

including an interface adjoint convective heat flux condition using the same heat transfer coefficient η . A fixed interface assumption was made to derive the above adjoint problem (as the design variable is knowingly constant in this setting), and we used the fact that the cost function does not depend explicitly on the wall quantities. A notable distinction between adjoint and state is the presence of a minus sign preceding the convective terms in the adjoint equations. This is evidence of the upstream convection of adjoint information, as opposed to the downstream convection of state, which proceeds from the non-normality of the Navier–Stokes operator [60]. Finally, we follow the line of thought in [61] and formulate the interface deformation as

$$\delta \mathbf{u} = \beta \nabla \mathbf{u} \cdot \mathbf{n}, \quad \delta T_f = \beta \nabla T_f \cdot \mathbf{n}, \quad (\text{A22})$$

and compute the one variation (encompassing the domain deformation, i.e., the interface is no longer assumed fixed) with respect to the design variable as

$$\begin{aligned} \delta_{\beta} J_s \equiv \delta_{\beta} \mathcal{L} = & \beta \int_{\Gamma} (\tilde{p} \mathbf{n} + 2\mu_f \boldsymbol{\varepsilon}(\tilde{\mathbf{u}}) \cdot \mathbf{n} + \rho_f c_{p_f} T_f \tilde{T}_f \mathbf{n}) \cdot (\nabla \mathbf{u} \cdot \mathbf{n}) \, ds \\ & + \beta \int_{\Gamma} k_f (\nabla \tilde{T}_f \cdot \mathbf{n}) (\nabla T_f \cdot \mathbf{n}) \, ds - \beta \int_{\Gamma} \tilde{T}_f (k_f \nabla (\nabla T_f \cdot \mathbf{n}) \cdot \mathbf{n}) \, ds. \end{aligned} \quad (\text{A23})$$

Since all solutions are incompressible, this ultimately reduces to

$$\begin{aligned} \delta_\beta J_s = & \beta \int_\Gamma \mu_f (\nabla \tilde{\mathbf{u}} \cdot \mathbf{n}) \cdot (\nabla \mathbf{u} \cdot \mathbf{n}) \, ds \\ & + \beta \int_\Gamma k_f (\nabla \tilde{T}_f \cdot \mathbf{n}) (\nabla T_f \cdot \mathbf{n}) \, ds - \beta \int_\Gamma \tilde{T}_f (k_f \nabla (\nabla T_f \cdot \mathbf{n}) \cdot \mathbf{n}) \, ds, \end{aligned} \tag{A24}$$

and the current steepest-descent algorithm progresses along the cost function, moving in the direction of the steepest slope using

$$\beta = -\mu_f (\nabla \tilde{\mathbf{u}} \cdot \mathbf{n}) \cdot (\nabla \mathbf{u} \cdot \mathbf{n}) - k_f (\nabla \tilde{T}_f \cdot \mathbf{n}) (\nabla T_f \cdot \mathbf{n}) + \tilde{T}_f (k_f \nabla (\nabla T_f \cdot \mathbf{n}) \cdot \mathbf{n}). \tag{A25}$$

Appendix A.2. Extension to the IVM-VMS Resolution Framework

In practical application, the heat transfer coefficient η ensuring that the fluid and solid exchange the proper amount of heat remains an unknown. Its determination remains quite a challenge, often necessitating the solution of an inverse problem to assimilate experimental data whose scarcity is widely recognized as a hindrance in practical applications (especially for topology optimization where varying the shape, amount, and distribution of the solid domain is integral to the optimization process itself). The underlying immersed volume method in this research blends both the fluid and solid phases into a single compound fluid with variable material properties. It thus solves Navier–Stokes and heat equations

$$\nabla \cdot \mathbf{u} = 0 \quad \text{in } \Omega, \tag{A26}$$

$$\rho \mathbf{u} \cdot \nabla \mathbf{u} = -\nabla p + \nabla \cdot (2\mu \boldsymbol{\varepsilon}(\mathbf{u})) \quad \text{in } \Omega, \tag{A27}$$

$$\rho c_p \mathbf{u} \cdot \nabla T = \nabla \cdot (k \nabla T) \quad \text{in } \Omega, \tag{A28}$$

identical to (A1)–(A3) but with varying density, viscosity, thermal conductivity and heat capacity, all accurately interpolated within a thin layer around the interface while otherwise being consistent with their respective fluid and solid properties. This allows dropping altogether the interface thermal condition (and thus alleviating the need for a heat transfer coefficient) because the amount of heat exchanged at the interface is entirely determined by the individual solid and fluid properties, hence the associated boundary conditions

$$\mathbf{u} = \mathbf{u}_i \quad \text{on } \Gamma_i, \tag{A29}$$

$$T = T_i \quad \text{on } \Gamma_i, \tag{A30}$$

$$\mathbf{u} = \mathbf{u}_o \quad \text{on } \Gamma_o, \tag{A31}$$

$$\nabla T \cdot \mathbf{n} = 0 \quad \text{on } \Gamma_o, \tag{A32}$$

$$\mathbf{u} = \mathbf{0} \quad \text{on } \Gamma_w^i \cup \Gamma_w^a, \tag{A33}$$

$$T = T_w \quad \text{on } \Gamma_w^i, \tag{A34}$$

$$\nabla T \cdot \mathbf{n} = 0 \quad \text{on } \Gamma_w^a. \tag{A35}$$

Provided the velocity in the solid domain is zero and the no-slip condition is satisfied at the interface, the convective term vanishes in (A28), and the solid equation reduces to a pure conduction problem, with prescribed temperature and zero heat flux conditions at the solid isothermal and adiabatic walls, respectively.

The exact same approach is applied to the adjoint equations by solving adjoint Navier–Stokes and heat equations

$$\nabla \cdot \tilde{\mathbf{u}} = 0 \quad \text{in } \Omega, \tag{A36}$$

$$-\rho \mathbf{u} \cdot \nabla \tilde{\mathbf{u}} + \rho \nabla \mathbf{u}^T \cdot \tilde{\mathbf{u}} = \nabla \tilde{p} + \nabla \cdot (2\mu \boldsymbol{\varepsilon}(\tilde{\mathbf{u}})) + \rho c_p T \nabla \tilde{T} \quad \text{in } \Omega, \tag{A37}$$

$$-c_p \mathbf{u} \cdot \nabla \tilde{T} = \nabla \cdot (k \nabla \tilde{T}) \quad \text{in } \Omega, \tag{A38}$$

identical to (A13)–(A15) but with variable density, viscosity, thermal heat capacity and thermal conductivity, together with boundary conditions

$$\tilde{\mathbf{u}} = -\partial_p J \mathbf{n} \quad \text{on } \Gamma_i, \tag{A39}$$

$$\tilde{T} = 0 \quad \text{on } \Gamma_i, \tag{A40}$$

$$\tilde{\mathbf{u}} = -\partial_p J \mathbf{n} \quad \text{on } \Gamma_o, \tag{A41}$$

$$k \nabla \tilde{T} \cdot \mathbf{n} + \rho c_p (\mathbf{u} \cdot \mathbf{n}) \tilde{T} = -\partial_T J \quad \text{on } \Gamma_o, \tag{A42}$$

$$\tilde{\mathbf{u}} = \mathbf{0} \quad \text{on } \Gamma_w^i \cup \Gamma_w^a, \tag{A43}$$

$$\tilde{T} = 0 \quad \text{on } \Gamma_w^i, \tag{A44}$$

$$\nabla \tilde{T} \cdot \mathbf{n} = 0 \quad \text{on } \Gamma_w^a. \tag{A45}$$

Assuming the adjoint velocity is zero in the solid domain (again this is hard-coded in the present context of extremely stretched, anisotropic mesh elements), Equation (A38) reduces to the pure conduction equation for the solid with zero adjoint temperature at the solid isothermal walls and zero adjoint heat flux at the solid adiabatic walls, just as what would be obtained by adding the solid conduction equation to the Lagrangian (A10) and evaluating the variation with respect to the state variables. Finally, we compute the steepest-descent displacement as

$$\beta = -\mu (\nabla \tilde{\mathbf{u}} \cdot \mathbf{n}) \cdot (\nabla \mathbf{u} \cdot \mathbf{n}) - k (\nabla \tilde{T} \cdot \mathbf{n}) (\nabla T \cdot \mathbf{n}) + \tilde{T} (k \nabla (\nabla T \cdot \mathbf{n}) \cdot \mathbf{n}). \tag{A46}$$

Since $\nabla(\mathbf{n} \cdot \mathbf{n}) = 0$ due to the normal vector having unit norm, it can be shown that

$$\nabla (\nabla T \cdot \mathbf{n}) \cdot \mathbf{n} = (\nabla (\nabla T) \cdot \mathbf{n}) \cdot \mathbf{n} + (\nabla \wedge \mathbf{n}) \cdot (\mathbf{n} \wedge \nabla T), \tag{A47}$$

and thus

$$\nabla (\nabla T \cdot \mathbf{n}) \cdot \mathbf{n} = (\nabla \wedge \mathbf{n}) \cdot (\mathbf{n} \wedge \nabla T), \tag{A48}$$

because the second derivatives vanish due to the use of P1 linear finite element approximations. Also, introducing H as the Hessian of ϕ , we have

$$\nabla \left(\frac{\phi}{\|\nabla \phi\|} \right) = \mathbf{n} - \frac{\phi}{\|\nabla \phi\|^3} H(\phi) \cdot \nabla \phi, \tag{A49}$$

on behalf of the normal vector in a level set setting being calculated as $\mathbf{n} = \nabla \phi / \|\nabla \phi\|$. Since the interface is by definition the zero iso-value of the level set, we thus have

$$\nabla \wedge \mathbf{n} = \nabla \wedge \nabla \left(\frac{\phi}{\|\nabla \phi\|} \right) = \mathbf{0}. \tag{A50}$$

It follows that

$$\nabla (\nabla T \cdot \mathbf{n}) \cdot \mathbf{n} \equiv 0, \tag{A51}$$

and Equation (A46) reduces to

$$\beta = -\mu (\nabla \tilde{\mathbf{u}} \cdot \mathbf{n}) \cdot (\nabla \mathbf{u} \cdot \mathbf{n}) - k (\nabla \tilde{T} \cdot \mathbf{n}) (\nabla T \cdot \mathbf{n}). \tag{A52}$$

The last step in the process is to specify the state derivatives of the cost function, that, for the present linear weighted sum of dissipated power (hydraulic component) and recoverable thermal power (thermal component), are given by

$$\partial_q J = (1 - \omega) \partial_q J_v - \omega \partial_q J_\Theta, \tag{A53}$$

with

$$\partial_p J_V = \mathbf{u} \cdot \mathbf{n}, \quad \partial_p J_\Theta = 0, \quad (\text{A54})$$

$$\partial_{\mathbf{u}} J_V = p_{tot} \mathbf{n} + \rho(\mathbf{u} \cdot \mathbf{n}) \mathbf{u}, \quad \partial_{\mathbf{u}} J_\Theta = \rho c_p T \mathbf{n}, \quad (\text{A55})$$

$$\partial_T J_V = 0, \quad \partial_T J_\Theta = \rho c_p (\mathbf{u} \cdot \mathbf{n}). \quad (\text{A56})$$

Appendix B. Coarse-Scale VMS Variational Problems

In this second appendix, the focus is on the stabilized finite element method employed for computing all relevant solutions on anisotropic adapted meshes and updating the layouts. To maintain simplicity in notation (without introducing ambiguity), we disregard the dependency of all variables on the optimization iteration, as well as the distinction between the continuous variables (operators, solutions, domains) and their finite element approximations. In practice, we solve the state equations in a sequential manner, meaning that the Navier–Stokes equations are solved first, and that the resulting velocity is used to solve subsequently the heat equation. Due to the reversal in space–time directionality (and thus in causality), the adjoint equations are also solved sequentially but in reverse order, i.e., we solve first the adjoint heat equation, then use the resulting adjoint temperature to solve the adjoint Navier–Stokes equations.

Appendix B.1. Navier–Stokes Equations

We obtain the state by time-stepping the time-dependent Navier–Stokes equations, using large time steps to expedite convergence towards a steady state (which occurs when the L-infinity norm of the difference between two consecutive solutions falls below 10^{-6}). In practice, we accommodate the time-dependency and non-linearity of the momentum equation by assuming the transport time scale to be much smaller for the fine scale than for the coarse scale. This allows to disregard the tracking in time of the fine scale (though it nonetheless displays quasi-static temporal variations, as it remains influenced by the time-dependent, coarse-scale residuals) and its contribution to the transport velocity. For technical and mathematical insights, along with detailed discussions on the validity of these approximations, refer to [62]. Ultimately, the coarse-scale variational problem reads

$$\int_{\Omega} (\rho \partial_t \mathbf{u} + \rho \mathbf{u} \cdot \nabla \mathbf{u}) \cdot \mathbf{w} \, dv + \int_{\Omega} 2\mu \boldsymbol{\varepsilon}(\mathbf{u}) : \boldsymbol{\varepsilon}(\mathbf{w}) \, dv - \int_{\Omega} p(\nabla \cdot \mathbf{w}) \, dv + \int_{\Omega} (\nabla \cdot \mathbf{u}) q \, dv - \sum_{k=1}^{N_e} \int_{\Omega_k} \tau_1 \mathbf{r}_1 \cdot (\rho \mathbf{u} \cdot \nabla \mathbf{w}) \, dv - \sum_{k=1}^{N_e} \int_{\Omega_k} \tau_1 \mathbf{r}_1 \cdot \nabla q \, dv - \sum_{k=1}^{N_e} \int_{\Omega_k} \tau_2 r_2 (\nabla \cdot \mathbf{w}) \, dv = 0. \quad (\text{A57})$$

Here, we denote by \mathbf{r}_1 and r_2 the large-scale residuals for the momentum and continuity equations expressed as

$$-\mathbf{r}_1 = \rho \partial_t \mathbf{u} + \rho \mathbf{u} \cdot \nabla \mathbf{u} + \nabla p, \quad -r_2 = \nabla \cdot \mathbf{u}, \quad (\text{A58})$$

whose second-order derivatives are zero because the spatial discretization scheme employs only linear interpolation functions. Additionally, Ω_k is the domain associated with the k th mesh element, where we assume the overall domain Ω to be discretized into N_e non-overlapping tetrahedrons (3-D) or triangles (2-D). Finally, the stabilization coefficients τ_2 and τ_1 are taken from previous works [42,63]. They are constants per mesh elements, and calculated based on characteristic velocity u and length h , defined, respectively, as the average L-2 norm of the nodal velocities, and the size of the mesh element in the velocity direction [64]. First-order accuracy in the time discretization of Equation (A57) is used that combines an implicit scheme for the conduction and the convection terms (in which the transport velocity is considered known) and an explicit scheme for the stabilization coefficients.

Appendix B.2. Heat Equation

The coarse-scale variational problem for the heat equation reads

$$\int_{\Omega} (\rho c_p \mathbf{u} \cdot \nabla T) s \, dv + \int_{\Omega} k \nabla T \cdot \nabla s \, dv - \sum_{k=1}^{N_e} \int_{\Omega_k} \tau_3 r_3 \rho c_p \mathbf{u} \cdot \nabla s \, dv - \sum_{k=1}^{N_e} \int_{\Omega_k} \tau_4 r_3 \rho c_p \mathbf{u}_{\parallel} \cdot \nabla s \, dv = 0, \tag{A59}$$

with

$$\mathbf{u}_{\parallel} = \frac{\mathbf{u} \cdot \nabla T}{\|\nabla T\|^2} \nabla T, \tag{A60}$$

the normalized projection of the velocity in the temperature gradient direction, r_3 is the large-scale residual of the heat equation

$$-r_3 = \rho c_p \mathbf{u} \cdot \nabla T, \tag{A61}$$

and $\tau_{3,4}$ are stabilization parameters defined in previous work [65,66], that operate in the direction of both the solution and its gradient. The discretization of Equation (A57) is first-order accurate in time, and combines an implicit scheme for the conduction and the convection terms (given that the convection velocity is considered known) and an explicit scheme for the stabilization coefficients.

Appendix B.3. Adjoint Heat Equation

Since the adjoint heat Equation (9) is formally identical to its state counterpart (save for the change in the sign of the convection velocity), its coarse-scale variational problem is deduced straightforwardly as

$$-\int_{\Omega} (\rho c_p \mathbf{u} \cdot \nabla T) s \, dv + \int_{\Omega} k \nabla T \cdot \nabla s \, dv + \sum_{k=1}^{N_e} \int_{\Omega_k} \tau_3 r_3 \rho c_p \mathbf{u} \cdot \nabla s \, dv + \sum_{k=1}^{N_e} \int_{\Omega_k} \tau_4 r_3 \rho c_p \mathbf{u}_{\parallel} \cdot \nabla s \, dv - \int_{\Gamma_o} \rho (\mathbf{u} \cdot \mathbf{n}) \tilde{T} s \, ds = \int_{\Gamma_o} \partial_T J s \, ds, \tag{A62}$$

and features the same residual r_3 and stabilization coefficients $\tau_{3,4}$ as in Appendix B.2. Note that Equation (A62) features additional integrals over the outlet elements. Those show up when applying integration by parts to the conduction term, which generates the boundary term

$$\int_{\partial\Omega} (k \nabla T \cdot \mathbf{n}) s \, ds = - \int_{\Gamma_o} (\rho (\mathbf{u} \cdot \mathbf{n}) \tilde{T} + \partial_T J) s \, ds, \tag{A63}$$

due to the adjoint outflow thermal condition (A19). In practice, though, preliminary tests have assessed that the adjoint thermal power term $\rho c_p (\mathbf{u} \cdot \mathbf{n}) \tilde{T}$ consistently dominates by at least four orders of magnitude over the heat flux term $k \nabla \tilde{T} \cdot \mathbf{n}$. We thus end up simplifying the numerical implementation using the approximate condition

$$\tilde{T} = -\omega \quad \text{on } \Gamma_o, \tag{A64}$$

and solve the scale variational problem (without a boundary term)

$$-\int_{\Omega} (\rho c_p \mathbf{u} \cdot \nabla T) s \, dv + \int_{\Omega} k \nabla T \cdot \nabla s \, dv + \sum_{k=1}^{N_e} \int_{\Omega_k} \tau_3 r_3 \rho c_p \mathbf{u} \cdot \nabla s \, dv + \sum_{k=1}^{N_e} \int_{\Omega_k} \tau_4 r_3 \rho c_p \mathbf{u}_{\parallel} \cdot \nabla s \, dv = 0, \tag{A65}$$

with an implicit scheme for the conduction and the convection terms and an explicit scheme for the stabilization coefficients.

Appendix B.4. Adjoint Navier–Stokes Equations

Following the main steps outlined in Appendix B.1, the following coarse-scale variational problem for the adjoint Navier–Stokes equations is obtained:

$$\begin{aligned} & \int_{\Omega} (-\rho \mathbf{u} \cdot \nabla \tilde{\mathbf{u}} + \rho \nabla \mathbf{u}^T \cdot \tilde{\mathbf{u}}) \cdot \mathbf{w} \, dv + \int_{\Omega} 2\mu \boldsymbol{\varepsilon}(\tilde{\mathbf{u}}) : \boldsymbol{\varepsilon}(\mathbf{w}) \, dv \\ & + \int_{\Omega} \tilde{p}(\nabla \cdot \mathbf{w}) \, dv - \int_{\Omega} \rho c_p T \nabla \tilde{T} \cdot \mathbf{w} \, dv + \int_{\Omega} (\nabla \cdot \tilde{\mathbf{u}}) q \, dv \\ & - \sum_{k=1}^{N_e} \int_{\Omega_k} \tau_1 \tilde{\mathbf{r}}_1 \cdot (-\rho \mathbf{u} \cdot \nabla \mathbf{w}) \, dv - \sum_{k=1}^{N_e} \int_{\Omega_k} \tau_1 \tilde{\mathbf{r}}_1 \cdot \nabla q \, dv - \sum_{k=1}^{N_e} \int_{\Omega_k} \tau_2 \tilde{r}_2 (\nabla \cdot \mathbf{w}) \, dv = 0. \end{aligned} \tag{A66}$$

whose large-scale residual terms read

$$-\tilde{\mathbf{r}}_1 = -\rho \mathbf{u} \cdot \nabla \tilde{\mathbf{u}} + \rho \nabla \mathbf{u}^T \cdot \tilde{\mathbf{u}} - \nabla \tilde{p}, \quad -\tilde{r}_2 = \nabla \cdot \tilde{\mathbf{u}}, \tag{A67}$$

and the stabilization coefficients $\tau_{1,2}$ are the same as those in Appendix B.1. This implicitly amounts to neglecting the additional stabilization stemming from the $\rho \nabla \mathbf{u}^T \cdot \tilde{\mathbf{u}}$ term describing the production of adjoint perturbations, that has been found to have no effect on the numerical results, as the problems considered herein are in the convection (not reaction) dominated limit.

Appendix B.5. Convective Level Set Method

We solve the auto-reinitialization level set problem defined in Equation (15) with an SUPG-type stabilization modeled after that of the convection–diffusion–reaction equation [67,68]. This yields the variational problem

$$\int_{\Omega} (\partial_{\tau} \phi + \mathbf{a}_{\tau} \cdot \nabla \phi) \zeta \, dv - \int_{\Omega_k} \tau_5 r_5 \mathbf{a}_{\tau} \cdot \nabla \zeta \, dv = \int_{\Omega} S \zeta \, dv, \tag{A68}$$

with residual

$$-r_5 = \partial_{\tau} \phi + \mathbf{a}_{\tau} \cdot \nabla \phi - S, \tag{A69}$$

and stabilization coefficient defined in the convection-dominated limit in [63]. It can be readily verified that all terms scale as $1/\Delta\tau$, allowing us to arbitrarily set the pseudo-time step value to $\Delta\tau = 1$ without compromising generality. The time discretization of Equation (A68) combines a semi-implicit scheme for the convection term (given that the transport velocity \mathbf{a}_{τ} depends on ϕ) and an explicit scheme for the stabilization coefficients and the source term.

References

1. Bendsøe, M.P.; Kikuchi, N. Generating optimal topologies in structural design using a homogenization method. *Comput. Methods Appl. Mech. Eng.* **1988**, *71*, 197–224. [[CrossRef](#)]
2. Bendsøe, M.P.; Sigmund, O. *Topology Optimization: Theory, Methods, and Applications*; Springer Science & Business Media: Berlin/Heidelberg, Germany, 2003.
3. Yang, R.J.; Chahande, A.I. Automotive applications of topology optimization. *Struct. Opt.* **1995**, *9*, 245–249. [[CrossRef](#)]
4. Zhu, J.H.; Zhang, W.H.; Xia, L. Topology optimization in aircraft and aerospace structures design. *Arch. Comput. Methods Eng.* **2016**, *23*, 595–622. [[CrossRef](#)]
5. Sigmund, O.; Maute, K. Topology optimization approaches. *Struct. Multidiscipl. Optim.* **2013**, *48*, 1031–1055. [[CrossRef](#)]
6. Deaton, J.D.; Grandhi, R.V. A survey of structural and multidisciplinary continuum topology optimization: Post 2000. *Struct. Multidiscipl. Optim.* **2014**, *49*, 1–38. [[CrossRef](#)]
7. Suzuki, K.; Kikuchi, N. A homogenization method for shape and topology optimization. *Comput. Methods Appl. Mech. Eng.* **1991**, *93*, 291–318. [[CrossRef](#)]

8. Allaire, G.; Bonnetier, E.; Francfort, G.; Jouve, F. Shape optimization by the homogenization method. *Numer. Math.* **1997**, *76*, 27–68. [[CrossRef](#)]
9. Sethian, J.A.; Wiegmann, A. Structural boundary design via level set and immersed interface methods. *J. Comput. Phys.* **2000**, *163*, 489–528. [[CrossRef](#)]
10. Wang, M.Y.; Wang, X.; Guo, D. A level set method for structural topology optimization. *Comput. Methods Appl. Mech. Eng.* **2003**, *192*, 227–246. [[CrossRef](#)]
11. Allaire, G.; Jouve, F.; Toader, A.M. Structural optimization using sensitivity analysis and a level-set method. *J. Comput. Phys.* **2004**, *194*, 363–393. [[CrossRef](#)]
12. Van Dijk, N.P.; Maute, K.; Langelaar, M.; Van Keulen, F. Level-set methods for structural topology optimization: A review. *Struct. Multidiscipl. Optim.* **2013**, *48*, 437–472. [[CrossRef](#)]
13. Dbouk, T. A review about the engineering design of optimal heat transfer systems using topology optimization. *Appl. Therm. Eng.* **2017**, *112*, 841–854. [[CrossRef](#)]
14. Alexandersen, J.; Andreasen, C.S. A review of topology optimisation for fluid-based problems. *Fluids* **2020**, *5*, 29. [[CrossRef](#)]
15. Yaji, K.; Yamada, T.; Kubo, S.; Izui, K.; Nishiwaki, S. A topology optimization method for a coupled thermal–fluid problem using level set boundary expressions. *Int. J. Heat Mass Transf.* **2015**, *81*, 878–888. [[CrossRef](#)]
16. Coffin, P.; Maute, K. Level set topology optimization of cooling and heating devices using a simplified convection model. *Struct. Multidiscipl. Optim.* **2016**, *53*, 985–1003. [[CrossRef](#)]
17. Feppon, F.; Allaire, G.; Dapogny, C.; Jolivet, P. Topology optimization of thermal fluid–structure systems using body-fitted meshes and parallel computing. *J. Comput. Phys.* **2020**, *417*, 109574. [[CrossRef](#)]
18. Dede, E.M. Multiphysics Topology Optimization of Heat Transfer and Fluid Flow Systems. In Proceedings of the COMSOL Users Conference, Boston, MA, USA, 30 March 2009.
19. Yoon, G.H. Topological design of heat dissipating structure with forced convective heat transfer. *J. Mech. Sci. Technol.* **2010**, *24*, 1225–1233. [[CrossRef](#)]
20. Marck, G. Optimisation Topologique des Transferts de Chaleur et de Masse: Application Aux échangeurs de Chaleur. Ph.D. Thesis, Ecole Nationale Supérieure des Mines de Paris, Paris, France, 2012.
21. Kontoleon, E.A.; Papoutsis-Kiachagias, E.M.; Zymaris, A.S.; Papadimitriou, D.I.; Giannakoglou, K.C. Adjoint-based constrained topology optimization for viscous flows, including heat transfer. *Eng. Optim.* **2013**, *45*, 941–961. [[CrossRef](#)]
22. Matsumori, T.; Kondoh, T.; Kawamoto, A.; Nomura, T. Topology optimization for fluid–thermal interaction problems under constant input power. *Struct. Multidiscipl. Optim.* **2013**, *47*, 571–581. [[CrossRef](#)]
23. Alexandersen, J.; Aage, N.; Andreasen, C.; Sigmund, O. Topology optimisation for natural convection problems. *Int. J. Numer. Methods Fluids* **2014**, *76*, 699–721. [[CrossRef](#)]
24. Qian, X.; Dede, E.M. Topology optimization of a coupled thermal-fluid system under a tangential thermal gradient constraint. *Struct. Multidiscipl. Optim.* **2016**, *54*, 531–551. [[CrossRef](#)]
25. Dugast, F.; Favennec, Y.; Josset, C.; Fan, Y.; Luo, L. Topology optimization of thermal fluid flows with an adjoint Lattice Boltzmann method. *J. Comput. Phys.* **2018**, *365*, 376–404. [[CrossRef](#)]
26. Subramaniam, V.; Dbouk, T.; Harion, J.L. Topology optimization of conjugate heat transfer systems: A competition between heat transfer enhancement and pressure drop reduction. *Int. J. Heat Fluid Flow* **2019**, *75*, 165–184. [[CrossRef](#)]
27. Duan, X.B.; Li, F.F.; Qin, X.Q. Adaptive mesh method for topology optimization of fluid flow. *Appl. Math. Lett.* **2015**, *44*, 40–44. [[CrossRef](#)]
28. Jensen, K.E. Topology optimization of Stokes flow on dynamic meshes using simple optimizers. *Comp. Fluids* **2018**, *174*, 66–77. [[CrossRef](#)]
29. Duan, X.B.; Qin, X.Q. Optimality criteria coupled adaptive mesh method for optimal shape design of Stokes flow. *Math. Methods Appl. Sci.* **2016**, *39*, 3910–3920. [[CrossRef](#)]
30. Duan, X.B.; Li, F.F.; Qin, X.Q. Topology optimization of incompressible Navier–Stokes problem by level set based adaptive mesh method. *Comput. Math. Appl.* **2016**, *72*, 1131–1141. [[CrossRef](#)]
31. Garcke, H.; Hecht, C.; Hinze, M.; Kahle, C. Numerical approximation of phase field based shape and topology optimization for fluids. *SIAM J. Sci. Comput.* **2015**, *37*, A1846–A1871. [[CrossRef](#)]
32. Feppon, F.; Allaire, G.; Bordeu, F.; Cortial, J.; Dapogny, C. Shape optimization of a coupled thermal fluid–structure problem in a level set mesh evolution framework. *SeMA* **2019**, *76*, 413–458. [[CrossRef](#)]
33. Feppon, F.; Allaire, G.; Dapogny, C.; Jolivet, P. Body-fitted topology optimization of 2D and 3D fluid-to-fluid heat exchangers. *Comput. Methods Appl. Mech. Eng.* **2021**, *376*, 113638. [[CrossRef](#)]
34. Alauzet, F.; Loseille, A. A decade of progress on anisotropic mesh adaptation for computational fluid dynamics. *Comput. Aided Des.* **2016**, *72*, 13–39. [[CrossRef](#)]
35. Sari, J.; Cremonesi, F.; Khalloufi, M.; Cauneau, F.; Meliga, P.; Mesri, Y.; Hachem, E. Anisotropic adaptive stabilized finite element solver for RANS models. *Int. J. Numer. Methods Fluids* **2018**, *86*, 717–736. [[CrossRef](#)]
36. Othmer, C. A continuous adjoint formulation for the computation of topological and surface sensitivities of ducted flows. *Int. J. Numer. Methods Fluids* **2008**, *58*, 861–877. [[CrossRef](#)]
37. Hinterberger, C.; Olesen, M. *Automatic Geometry Optimization of Exhaust Systems Based on Sensitivities Computed by a Continuous Adjoint CFD Method in OpenFOAM*; Technical Paper 2010-01-1278; SAE 2010 World Congress & Exhibition: Detroit, MI, USA, 2010.

38. Hinterberger, C.; Olesen, M. Industrial application of continuous adjoint flow solvers for the optimization of automotive exhaust systems. In Proceedings of the ECCOMAS Thematic Conference on CFD & Optimization Methods and Applications, Antalya, Turkey, 23–25 May 2011; pp. 1–17.
39. Zeng, S.; Kanargi, B.; Lee, P.S. Experimental and numerical investigation of a mini channel forced air heat sink designed by topology optimization. *Int. J. Heat Mass Transf.* **2018**, *121*, 663–679. [[CrossRef](#)]
40. Athan, T.W.; Papalambros, P.Y. A note on weighted criteria methods for compromise solutions in multi-objective optimization. *Eng. Optim.* **1996**, *27*, 155–176. [[CrossRef](#)]
41. Hachem, E.; Digonnet, H.; Massoni, E.; Coupez, T. Immersed volume method for solving natural convection, conduction and radiation of a hat-shaped disk inside a 3D enclosure. *Int. J. Numer. Methods Heat Fluid Flow* **2012**, *22*, 718–741. [[CrossRef](#)]
42. Hachem, E.; Feghali, S.; Codina, R.; Coupez, T. Immersed stress method for fluid-structure interaction using anisotropic mesh adaptation. *Int. J. Numer. Methods Eng.* **2013**, *94*, 805–825. [[CrossRef](#)]
43. Patankar, S.V. *Numerical Heat Transfer and Fluid Flow*; Taylor & Francis: Abingdon, UK, 1980.
44. Patankar, S.V. A numerical method for conduction in composite materials, flow in irregular geometries and conjugate heat transfer. In Proceedings of the 6th International Heat Transfer Conference, Toronto, ON, Canada, 7–11 August 1978; pp. 297–302.
45. Ville, L.; Silva, L.; Coupez, T. Convected level set method for the numerical simulation of fluid buckling. *Int. J. Numer. Methods Fluids* **2011**, *66*, 324–344. [[CrossRef](#)]
46. Coupez, T.; Silva, L.; Hachem, E. Implicit boundary and adaptive anisotropic meshing. In *New Challenges in Grid Generation and Adaptivity for Scientific Computing*; Perotto, S., Formaggia, L., Eds.; Springer: Berlin/Heidelberg, Germany, 2015; pp. 1–18.
47. Bonito, A.; Guermont, J.L.; Lee, S. Numerical simulations of bouncing jets. *Int. J. Numer. Methods Fluids* **2016**, *80*, 53–75. [[CrossRef](#)]
48. Coupez, T. Metric construction by length distribution tensor and edge based error for anisotropic adaptive meshing. *J. Comput. Phys.* **2011**, *230*, 2391–2405. [[CrossRef](#)]
49. Jannoun, G.; Hachem, E.; Veysset, J.; Coupez, T. Anisotropic meshing with time-stepping control for unsteady convection-dominated problems. *Appl. Math. Model.* **2015**, *39*, 1899–1916. [[CrossRef](#)]
50. Coupez, T. Génération de maillage et adaptation de maillage par optimisation locale. *Rev. Eur. Elem. Finis* **2000**, *9*, 403–423. [[CrossRef](#)]
51. Meliga, P.; Chomaz, J.M.; Sipp, D. Unsteadiness in the wake of disks and spheres: Instability, receptivity and control using direct and adjoint global stability analyses. *J. Fluids Struct.* **2009**, *25*, 601–616. [[CrossRef](#)]
52. Balay, S.; Abhyankar, S.; Adams, M.F.; Brown, J.; Brune, P.; Buschelman, K.; Dalcin, L.; Dener, A.; Eijkhout, V.; Gropp, W.; et al. *PETSc Users Manual (Rev. 3.13)*; Technical report ANL-95/11-Rev. 3.13; Argonne National Lab.: Lemont, IL, USA, 2020.
53. Marck, G.; Nemer, M.; Harion, J.L. Topology optimization of heat and mass transfer problems: laminar flow. *Numer. Heat Transf. Part Fundam.* **2013**, *63*, 508–539. [[CrossRef](#)]
54. Takagi, J.; Yamada, M.; Yasuda, M.; Seki, M. Continuous particle separation in a microchannel having asymmetrically arranged multiple branches. *Lab Chip* **2005**, *5*, 778–784. [[CrossRef](#)] [[PubMed](#)]
55. Liu, Z.; Gao, Q.; Zhang, P.; Xuan, M.; Wu, Y. Topology optimization of fluid channels with flow rate equality constraints. *Struct. Multidiscipl. Optim.* **2011**, *44*, 31–37. [[CrossRef](#)]
56. Zhou, T.; Liu, T.; Deng, Y.; Chen, L.; Qian, S.; Liu, Z. Design of microfluidic channel networks with specified output flow rates using the CFD-based optimization method. *Microfluid. Nanofluidics* **2017**, *21*, 11. [[CrossRef](#)]
57. Gargantini, G. Design of Bi-Fluid Heat Exchangers Using Topology Optimization. Master's Thesis, Politecnico di Milano, Milan, Italy, 2020.
58. Villanueva, C.H.; Maute, K. CutFEM topology optimization of 3D laminar incompressible flow problems. *Comput. Methods Appl. Mech. Eng.* **2017**, *320*, 444–473. [[CrossRef](#)]
59. Flageul, C.; Benhamadouche, S.; Lamballais, É.; Laurence, D. DNS of turbulent channel flow with conjugate heat transfer: Effect of thermal boundary conditions on the second moments and budgets. *Int. J. Heat Fluid Flow* **2015**, *55*, 34–44. [[CrossRef](#)]
60. Chomaz, J.M. Global instabilities in spatially developing flows: Non-normality and nonlinearity. *Annu. Rev. Fluids Mech.* **2005**, *37*, 357–392. [[CrossRef](#)]
61. Soto, O.; Löhner, R. On the computation of flow sensitivities from boundary integrals. In Proceedings of the 42nd AIAA Aerospace Sciences Meeting and Exhibit, Reno, NV, USA, 5–8 January 2004.
62. Hachem, E.; Rivaux, B.; Kloczko, T.; Digonnet, H.; Coupez, T. Stabilized finite element method for incompressible flows with high Reynolds number. *J. Comput. Phys.* **2010**, *229*, 8643–8665. [[CrossRef](#)]
63. Codina, R. Stabilized finite element approximation of transient incompressible flows using orthogonal subscales. *Comput. Methods Appl. Mech. Eng.* **2002**, *191*, 4295–4321. [[CrossRef](#)]
64. Tezduyar, T.; Osawa, Y. Finite element stabilization parameters computed from element matrices and vectors. *Comput. Methods Appl. Mech. Eng.* **2000**, *190*, 411–430. [[CrossRef](#)]
65. Brooks, A.; Hughes, T.J.R. Streamline upwind/Petrov–Galerkin formulations for convection dominated flows with particular emphasis on the incompressible Navier–Stokes equations. *Comput. Methods Appl. Mech. Eng.* **1982**, *32*, 199–259. [[CrossRef](#)]
66. Galeão, A.C.; Do Carmo, E.G.D. A consistent approximate upwind Petrov–Galerkin method for convection-dominated problems. *Comput. Methods Appl. Mech. Eng.* **1988**, *68*, 83–95. [[CrossRef](#)]

67. Codina, R. Comparison of some finite element methods for solving the diffusion-convection-reaction equation. *Comput. Methods Appl. Mech. Eng.* **1998**, *156*, 185–210. [[CrossRef](#)]
68. Badia, S.; Codina, R. Analysis of a stabilized finite element approximation of the transient convection-diffusion equation using an ALE framework. *SIAM J. Numer. Anal.* **2006**, *44*, 2159–2197. [[CrossRef](#)]

Disclaimer/Publisher’s Note: The statements, opinions and data contained in all publications are solely those of the individual author(s) and contributor(s) and not of MDPI and/or the editor(s). MDPI and/or the editor(s) disclaim responsibility for any injury to people or property resulting from any ideas, methods, instructions or products referred to in the content.